2017

Extraordinary Optical Transmission in Aligned Carbon Nanotube Devices at Terahertz Frequencies.

Shaikhah F. Almousa
Wright State University

EXTRAORDINARY OPTICAL TRANSMISSION IN ALIGNED CARBON NANOTUBE DEVICES AT TERAHERTZ FREQUENCIES

A thesis submitted in partial fulfillment of the

requirements for the degree of

Master of Science

By

SHAIKHAH F. ALMOUSA

B.S., King Saud University, 2011

2017

Wright State University

WRIGHT STATE UNIVERSITY

GRADUATE SCHOOL

April 18, 2017

I HEREBY RECOMMEND THAT THE THESIS PREPARED UNDER MY SUPERVISION BY Shaikhah F. Almousa ENTITLED Extraordinary Optical Transmission in Aligned Carbon Nanotube Devices at Terahertz Frequencies BE ACCEPTED IN PARTIAL FULFILLMENTOF THE REQUIREMENTS FOR THE DEGREE OF Master of Science.

_____

Jason A. Deibel, Ph.D.
Thesis Director

_____

Jason A. Deibel
Chair, Department of Physics

Committee on
Final Examination

_____

Jason Deibel, Ph.D.

_____

Brent Foy, Ph.D.

_____

Jerry Clark, Ph.D.

_____

Robert E. W. Fyffe, Ph.D.
Vice President for Research
and Dean of the Graduate School

ABSTRACT

Almousa, Shaikhah F. M.S. Department of Physics, Wright State University, 2017. Extraordinary Optical Transmission in Aligned Carbon Nanotube Devices at Terahertz Frequencies.

In the phenomenon known as extraordinary optical transmission (EOT), a narrow band of selected frequencies are transmitted when incident on an array of subwavelength periodic apertures where the resonant frequency is determined by the geometry of the array of apertures and optical properties of the metal-dielectric interface. This takes place due to the excitation of surface plasmon polaritons (SPPs) at the metal and dielectric interface. Using the COMSOL Multiphysics software RF Module, a unit cell of a carbon nanotube (CNT) based EOT device is modeled in order to verify theoretical calculations of the resonant frequency using S-parameter calculations. The simulation of the interaction of the THz light with the CNT EOT device exhibits a resonant transmission at 235 GHz. Further, the transmission falls exponentially with increasing device thickness of the device, and the transmission peak reaches its maximum value at the skin depth. Although some of the transmission features, such as Woods anomalies, are seen in the modeled device only, the other numerical results show good agreement with the experimental observations reported in literature. The fabricated single-walled carbon nanotube devices with 100 nm thickness do not indicate any resonances; however any such resonances might be weak due to the thin nature of the samples.

Contents

1 Introduction **1**

1.0.1 Outlines 4

2 Background **5**

2.1 Terahertz Spectroscopy 5

2.1.1 Generation and Detection of THz Beam Using Photoconductive Antenna 6

2.1.2 THz Time Domain Spectroscopy 7

2.2 Drude Model 11

2.2.1 Optical properties of materials 11

2.2.2 Limitation of Drude Model 13

2.3 Surface Plasmon Polaritons 13

2.4 Extraordinary Optical Transmission (EOT) 15

2.4.1 Time of Flight Model 17

2.4.2 Thickness of an EOT device 20

2.4.3 EOT of Carbon Nanotubes 22

3 Modeling of the EOT Device **24**

3.1 Modeling Technique 25

3.1.1 Geometry 26

3.1.2 Materials 26

3.1.3 Boundary Conditions 28

3.2 Analysis of the modeled EOT Device 30

3.2.1 Transmission Results 30

3.2.2 Transmission as a Function of Thickness 34

4 CNT EOT Device **40**

4.1 CNT-based EOT Device Fabrication Process 40

4.2 Analysis of CNT-based EOT device 41

5 Summary and Outlook **48**

Bibliography **50**

List of Figures

1.1 A transmission time domain THz image shows the contents of a laptop bag 3

1.2 (a) the couplin between the normal electric field in the surface of incident and the plasma near the surface in metal-dieletric interface where H is the magnetic field parallel to the surface. (b) The amplitude electric filed decays exponantially in both regions where $z > 0$ and $z < 0$ (6). 3

2.1 THz frequencies lie in the region between infrared and microwave frequencies (12). 6

2.2 A THz generation system consists of Ti:Sapphire femtosecond laser at a center wavelength= 800 nm and photon energy= 1.55 eV and two metal electrodes deposited on a GaAs photoconductive antenna with a bandgap= 1.42 eV (12). 7

2.3 The basic elements of a standard THz time domain system that are composed of two GaAs photoconductive antennas inside both the transmitter ”generator” and the receiver ”detector”, an ultrafast laser, and optical delay line (12). 8

2.4 A THz time domain transmission measurement from an arbitrary sample. . 9

2.5 A THz frequency domain transmission measurement from an arbitrary sample. 10

2.6 Dispersion relation of a metal-dielectric interface. 14

2.7 An incident wave with angle θ on an array of apertures of periodicity length L and rectangular apertures of width a and length b arranged in a square lattice. 16

2.8 The dispersion relation of a free-standing EOT device. The dotted line on the left is the light line. The curve is the SPPs dispersion curve intersected with two incident light shifted to the right from the light line due to the gained momentum in the two dimension array. The two shifted lines are for different frequency orders that have different m and n. 18

2.9 The quantity $\sqrt{\frac{\epsilon_m \epsilon_d}{\epsilon_m + \epsilon_d}}$ can be approximated to $\sqrt{\epsilon_d}$ at THz frequencies. For metal-air EOT device $\sqrt{\frac{\epsilon_m \epsilon_d}{\epsilon_m + \epsilon_d}}$ approaches 1, air dielectric constant, as $\frac{\omega}{\omega_p}$ approaches THz frequencies. 18

2.10 The time domain (on the left) and the frequency domain of transmission measurements (on the right) of copper-based EOT device. 20

2.11 The coupling (continuous red line) and decoupling (green line) of the incident polarized wave I perpendicular to the long side of the apertures represent the nearest event while the coupling and recoupling of the incident wave II perpendicular to the short side of the apertures represent the next nearest neighbor event. The direction of the electric field points to the preferred direction normal to the long side. 21

2.12 The real part (blue) and the imaginary part (green) of the refractive index as it is extracted from (10). 23

3.1 The power wave parameters. a_1 is the incident power wave on port 1, b_1 is the reflected power wave on port 1, a_2 is the incident power wave on port 2, b_2 is the reflected power wave on port 2. 26

3.2 The aperture dimensions and lattice arrangement of a unit cell of the copper-based EOT device of $50\,\mu\mathrm{m}$ thickness and peridicity length $L = 300\,\mu\mathrm{m}$. The rectangular apertures arranged in a triangular lattice have width of $40\,\mu\mathrm{m}$ and the length of $160\,\mu\mathrm{m}$. 27

3.3 The aperture dimensions and lattice arrangement of a unit cell of the CNT-based EOT device of $25\,\mu\mathrm{m}$ thickness and peridicity length L=1.2 mm. The circular apertures arranged in a square lattice have a diameter= 0.65 mm. . . 27
3.4 The PEC boundaries are chosen to be normal to the electric field polarization direction (along y) while the other sides are defined to be PMCs. This configuration yields an infinite plane wave and infinite periodic array. . . . 28
3.5 The skin depth of copper from 100 GHz to 3 THz. The skin depth has 1×10^{-7} order of magnitude at THz frequencies. 29
3.6 Meshing of both devices is defined by a physics controlled mesh with maximum element size equal to $\frac{\lambda}{6}$. The maximum element size of the IBC boundaries is defined to be less than the skin depth of both materials. 30
3.7 The magnitude of the S21-parameter of the copper-based EOT device exhibits a resonant frequency at 0.86 THz. The red line shows the low transmission through a copper wafer. 31
3.8 The transmitted wave through the copper-based EOT device at (a) 0.6 THz (b) the resonant frequency 0.86 THz. The wave is propagating from right to left. 31
3.9 The z-component of the electric field on the surface (xy plane) at (a) 0.86 THz of the copper-based EOT device (b) 0.235 THz of the CNT-based EOT device shows the coupling and propagating of the wave on the surface. The propagation of the surface wave cannot be seen at a lower frequency (c) 0.60 THz of the copper-based EOT device (d) 0.1 THz of the CNT-based EOT device. The intensity scale is the same for both images, and the same wave appears in both sides of the EOT device. 32
3.10 The magnitude of the S21-parameter of the CNT-based EOT device exhibits a resonant frequency at 0.235 THz. 33
3.11 The transmission of the CNT EOT device of multiple thicknesses ranging from 50 nm to $150\,\mu\mathrm{m}$. 34

3.12 3D graph of the transmission of the CNT EOT device of multiple thicknesses ranging from 50 nm to $150\,\mu\mathrm{m}$ and frequencies from 200 GHz to 300 GHz. 35
3.13 The transmission falls exponentially eith increasing the thickness for all three regions, pre resonance at 200 GHz, near resonance at 225 GHz, and post resonance at 255 THz. The exponential decay of wood's anamoly at 250 GHz is shown. 36
3.14 The decay coefficient α of the transmission as a function of the frequencies in pre-resonance, near resonance, and post-resonance regions. 37
3.15 The transmission peak as a function of the thickness has its maximum value at $40\,\mu\mathrm{m}$ close to the calculated skin depth. The simulation data is fitted to quadratic function. 38
3.16 The critical thickness where the resonantly enhanced transmission can no longer be seen appears at $448\,\mu\mathrm{m}$ calculated from the fitting results. 38
3.17 The transmission at the frequency 240 GHz followed the resonance directly shows a minimum transmission at the skin septh $40\,\mu\mathrm{m}$. 39

4.1 The first set (samples 1-3) has a circular aperture that arranged in square a lattice arrangement except for sample 2 that has a triangular lattice. The area of the first two samples of the first set are kept the same while the area of the third sample is about 50% bigger than the other samples of the same set. In the second set (samples4-6), all samples have rectangular apertures arranged in a square lattice except the second one of the same set that arranged in a triangular lattice. In this set, the area of the third sample is 50% less than the two samples of the same set. Samples 7-9, the circular apertures of the same area that arranged in a square lattice are separate by $L = 0.8, 0.6,$ and $0.5\ mm$ for samples 7, 8, and 9 respectively that are corresponding to 375, 500, and 600 GHz resonant frequency respectively. The area of this set is less than sample 1 by 50%. Each sample is centered in 11 mm by 11 mm square which fits the THz laser beam that has 10 mm diameter. 42

4.2 A scheme illustrates the THz transmission time domain spectroscopy. The THz beam size fits the EOT device. 43

4.3 The time-domain terahertz transmission spectroscopy measurements of the silicon substrate (reference) and sample 2 with two orientations that show the maximum and minimum transmission associated with the orientation of the CNT's 45

4.4 The time-domain terahertz transmission spectroscopy measurements of the silicon substrate (reference), sample 1, sample, 2, and sample 3. 45

4.5 The THz frequency domain transmission spectroscopy measurements of the silicon substrate (reference), sample 1, sample, 2, and sample 3. 46

4.6 The THz frequency domain transmission spectroscopy measurements normalized to reference of sample 1, sample, 2, and sample 3. 47

List of Tables

2.1 The plasma frequency ω_p and the collision frequency γ 12

4.1 Apertures shape and dimensions, lattice arrangement, area, and periodicity length for each sample. 43

Dedicated to my parents, Fahd and Joharah, my husband, Khalid,

my daughter, Joud, and our baby in the way.

Acknowledgments

I send my deepest acknowledgment to my parents at home, Saudi Arabia, for all the prayers, wishes, kind supportive words that have been pushing me to do my best in all my endeavors. A heartfelt gratitude to my soulmate for all the love, support, and collaboration that took me to this stage. My enormous thanks are for my three years and a half daughter for being with me during my master study. I am thankful to King Saud University for granting me a scholarship that has enabled me to pursue my higher degrees as one of its future professors.

I would like to greatly thank Dr. Jason Deibel for being my advisor for two years that enhanced my research skills experimentally and computationally in the Terahertz and Ultrafast Photonics Research laboratory at Wright State University. My deep appreciation is for Dr. Weilu Gao for fabricating my samples in Dr. Junichiro Kono laboratory at Rice University. I am greatly indebted to Dr. Brent Foy and Dr. Jerry Clark for the support, efforts they put in the unforgettable classes I had with them, and for being in my defense committee. I would like to thank Dr. Allen G. Hunt for his support, Dr. Adrienne Traxler for LaTeX help, and Dr. Weidong Zhang for his support in the layout software.

I am thankful to all of my family, friends, lab group who have been supporting and encouraging wishing me the best positions in life.

Chapter 1

Introduction

The terahertz gap of the electromagnetic spectrum lies between 100 GHz and 30 THz (1) and has been drawn significant attention in photonic research due to its capabilities associated with the characterization of materials properties, safety, and its ability to propagate in dielectrics creating further applications in security and medical biology (2) (Figure 1.1). The extensive progress of THz applications has stimulated research seeking more understanding of the behavior of materials in this regime and other fields such as plasmonics and quantum cascade lasers (1). Extraordinary optical transmission (EOT) in metallic subwavelength apertures has been observed in the THz region. The reason behind this transmission through an array of apertures is attributed to the propagation of a surface wave on the metal at a resonant frequency determined by the periodicity length of the array and both metal and dielectric relative permittivities (3). After surface plasmon polaritons (SPPs) are initiated at the aperture edges when light is incident on the metal surface, they propagate along the surface of the metal and then decouple into free space and recouple at the apertures

edges (4). The SPPs are a coupling between electromagnetic waves and the free electrons near the surface at a metal-dielectric interfaces. For a transverse magnetic (TM) polarized electromagnetic wave where the electric field is normal to the surface of incident, oscillating accumulated charges trap the wave at the surface (5). Solving Maxwells equations for a flat dielectric-metal interface shows that the electric field decays exponentially in the normal direction to the surface giving a strong field close to the surface as illustrated in Figure 1.2 (6). This feature makes the SPPs a useful technique in detection purposes (7). As many critical materials have resonances at THz frequencies such as semiconductors and bioligical components such as proteins (7), SPPs excitation techniques draw significant attention to exploit the strong field in spectroscopic and sensing applications. Although such a transmission has been observed 1998 (8), there is no unified theory that fully explains the enhancement of the transmitted low frequency light through two-dimensional aperture arrays (4). According to the time-of- flight qualitative model, the polarization direction and the geometry of the thin film apertures such as the dimensions, shape and area notably contribute to the resonance of the transmitted wave (4). The geometry of the most enhanced transmission reported for a copper thin film that had asymmetric apertures (4) was further used to show the transmission with a carbon nanotube (CNT) based EOT on a silicon substrate (9). However, the transmission for the case of a free standing CNT-based EOT was shown to have a more enhanced transmission through symmetric apertures (10) and was broadband with symmetric apertures on a silicon substrate (11). The facility of simulating EOT devices as a function of various geometries of the apertures array as well as the material properties could lead to better understanding of the EOT devices. Using the COMSOL Multiphysics. RF module, a copper- based EOT is simulated as a preliminary model that shows good agreement with the experiment. The free standing CNT-based EOT devices is simulated and investigated as a function of thickness.

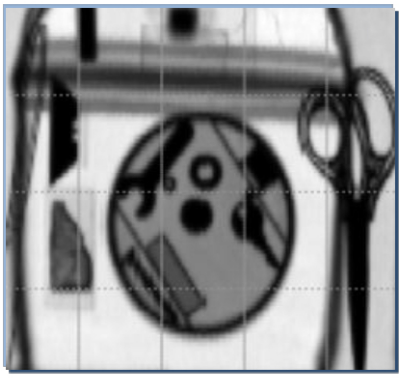

Figure 1.1: A transmission time domain THz image shows the contents of a laptop bag

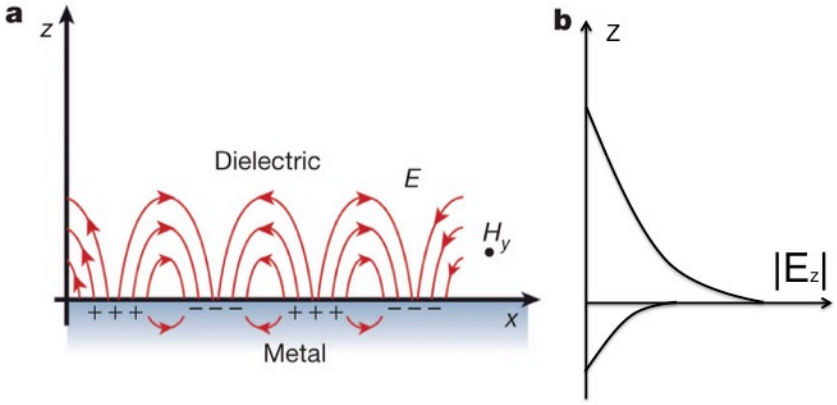

Figure 1.2: (a) the couplin between the normal electric field in the surface of incident and the plasma near the surface in metal-dieletric interface where H is the magnetic field parallel to the surface. (b) The amplitude electric filed decays exponantially in both regions where $z > 0$ and $z < 0$ (6).

1.0.1 Outlines

In the second chapter of this thesis, the background needed to perform both simulation and experimental work will be covered starting from a general description of THz radiation followed by the methodology of generating and detection of THz waves. As THz time domain spectroscopy is used to study the optical properties of samples under investigation, it is illustrated as the end of this section. Further, the Drude model that describes the optical properties of materials theoretically is described with the fundamental relations used in the simulation. The validation of using the Drude model is presented at the end of this section. The Drude model is followed by a classical description of SPPs and the dispersion relation followed by the theoretical representation of EOT that is described using the Time of Flight Model. Literature studies of the effects of changing thickness and CNT EOT are presented at the end of this chapter.

The third chapter starts with a description of using the Finite Element Method as a numerical method used in electromagnetic simulations. The modeling method is presented in this chapter covering the geometry, boundary conditions, and materials used in the simulation of the copper-based EOT device as a preliminary study as well as CNT-based EOT device. The simulation results of the transmission as a function of thickness are discussed at the end of the chapter.

In chapter 4, transmission properties of the fabricated CNT-EOT device are investigated with changing the lattice arrangement and the area. This is presented after a description of the fabrication process. The thesis is ended by a brief summary and outlook of the future work.

Chapter 2

Background

2.1 Terahertz Spectroscopy

The Terahertz gap of the electromagnetic spectrum lies between 100 GHz and 30 THz (1) between the infrared and microwave frequencies as shown in Figure 2.1 (12). Besides the safety of the THz electromagnetic waves due to their low photon energy, THz radiation is promosing for transmission through dielectrics, such as plastic and clothes, stimulating extensive THz sensing and imaging applications in security and medical biology (2). On the other hand, metals are highly reflective at THz frequencies. Although efficient THz generation and detection methods were not available until 1980 (13), nowadays, THz beams can be generated and detected by various ways. In this section, we will focus on utilizing photoconductive antenna techniques as the generation and detection method used in this work.

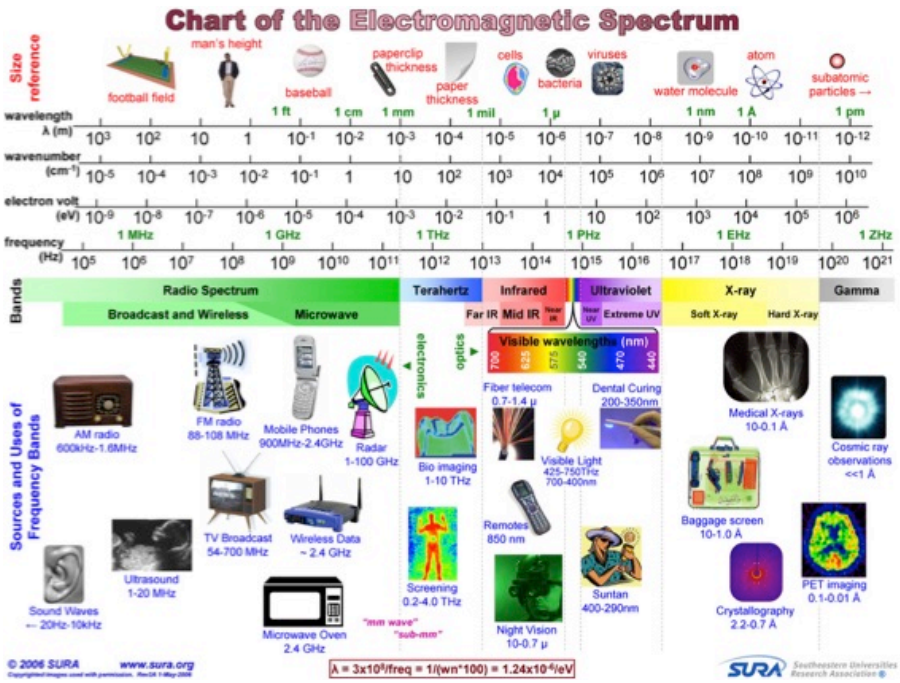

Figure 2.1: THz frequencies lie in the region between infrared and microwave frequencies (12).

2.1.1 Generation and Detection of THz Beam Using Photoconductive Antenna

The standard system that generates a pulsed THz beam consists of two GaAs photoconductive antennas, one for generation while the other for detection, an ultrafast laser, an optical delay line, and mirrors and lenses to split, collimate, and focus the beam. The Ti:Sapphire femtosecond laser with a center wavelength of 800 nm is split into pump and probe beams associated with the generation and detection respectively. When the pump beam hits the GaAs photoconductive antenna that consists of two metal electrodes seperated by a $5\,\mu\mathrm{m}$ to $100\,\mu\mathrm{m}$ gap, it excites electron-hole pairs. The THz beam radiates when a DC voltage is applied across the electrodes as shown in Figure 2.2 (12). The probe beam that passes the optical delay path excites electron-hole pairs as well in the other photoconductive antenna. The electron hole pairs are accelerated by the generated THz beam creating a time varying current. The optical delay line consists of mirrors and a mechanical scanner that moves to

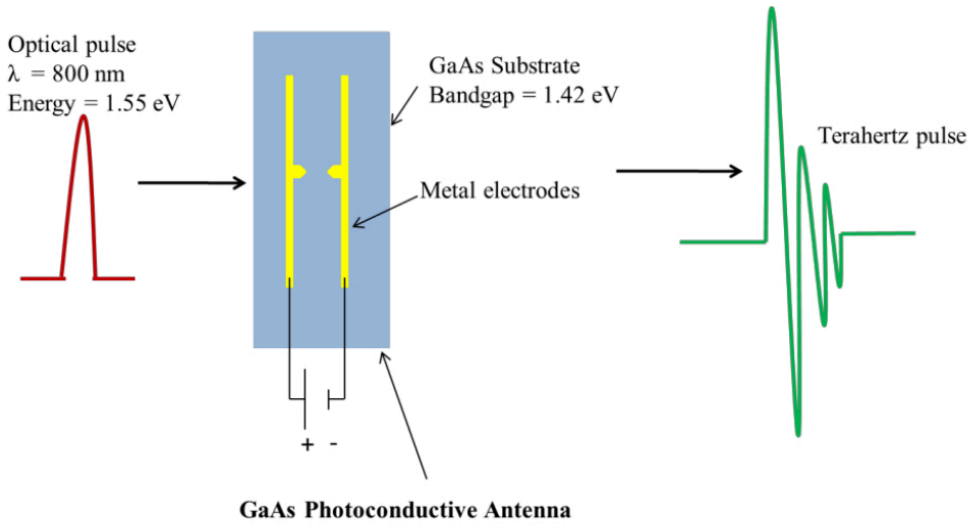

Figure 2.2: A THz generation system consists of Ti:Sapphire femtosecond laser at a center wavelength= 800 nm and photon energy= 1.55 eV and two metal electrodes deposited on a GaAs photoconductive antenna with a bandgap= 1.42 eV (12).

detect the THz signal as a function of the time delay, THz time domain or THz temporal waveform. In THz imaging, the THz time domain is taken for each spacial point creating a THz image for an entire sample (2; 14). A standard THz system is shown in Figure 2.3 (12).

2.1.2 THz Time Domain Spectroscopy

A THz time domain spectroscopy system utilizes the time domain THz signal of a sample to calculate the optical properties of the sample such as the refractive index and the absorption coefficient measurements. In order to investigate the frequency dependent properties, the time domain can be transformed to the frequency domain yielding both the amplitude and the phase of the signal using Fast Fourier Transformation (12). The time and frequency domain are shown in Figure 2.4 and 2.5 for an arbitrary sample.

The refractive index n and the absorption coefficient α can be calculated using the

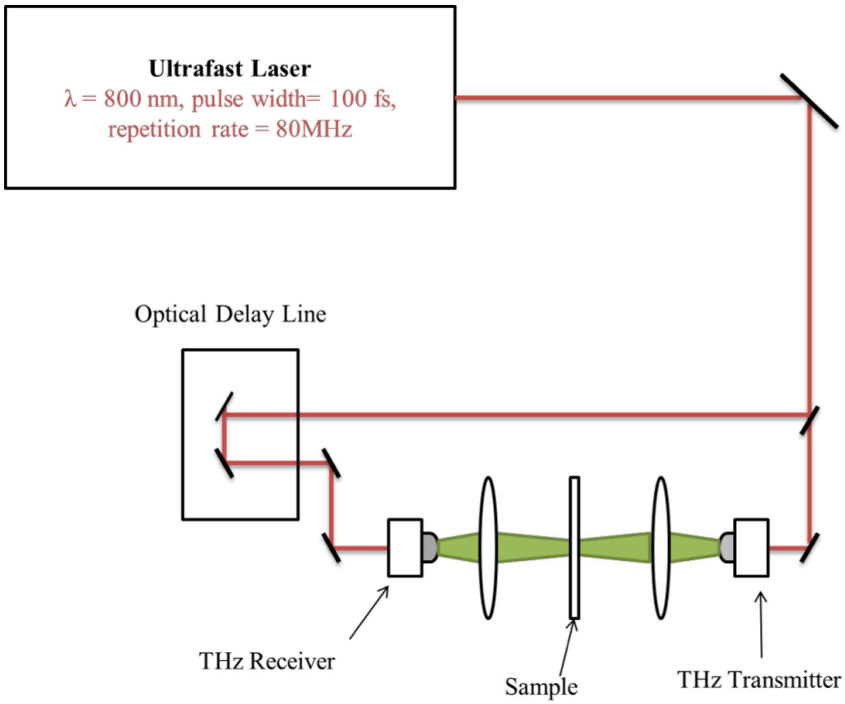

Figure 2.3: The basic elements of a standard THz time domain system that are composed of two GaAs photoconductive antennas inside both the transmitter ”generator” and the receiver ”detector”, an ultrafast laser, and optical delay line (12).

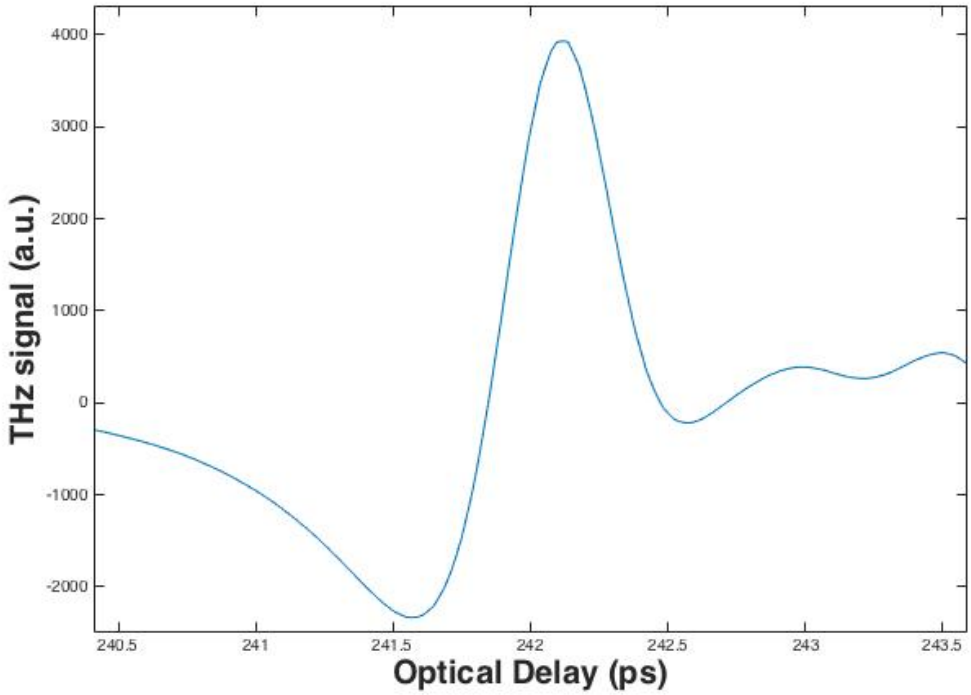

Figure 2.4: A THz time domain transmission measurement from an arbitrary sample.

following relations (12)

$$\alpha d = -20log[\frac{A_s}{A_r}/T(n)] \tag{2.1}$$

$$nd = 1 + \frac{c}{\omega}(\phi_s - \phi_r) \tag{2.2}$$

where A_s and ϕ_s are the electric field amplitude and phase respectively after the transmission through the sample, A_r and ϕ_r are the electric field amplitude and phase before the transmission, $T(n)$ is the Frensel reflection at the surface, d is the sample thickness, ω is the angular frequency of the incident wave, and c is the speed of light (12).

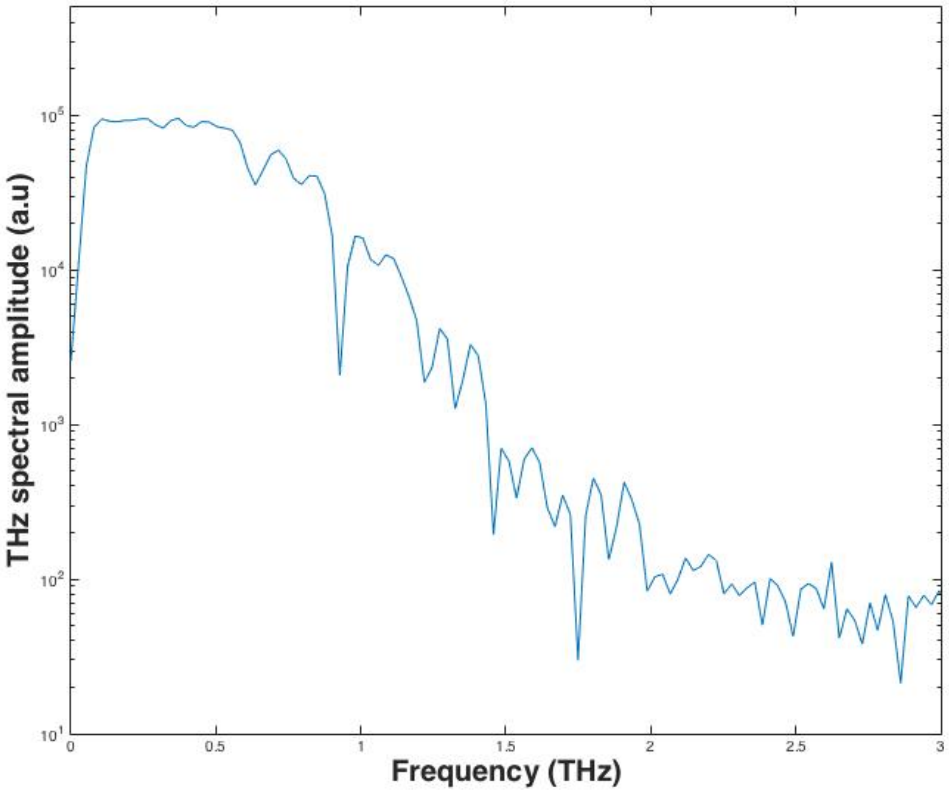

Figure 2.5: A THz frequency domain transmission measurement from an arbitrary sample.

2.2 Drude Model

In this section, the Drude model that describes the optical properties of metals is reviewed as the model used in the simulation part of this work. The mathematical description of the optical properties, such as the dielectric constant and AC conductivity are presented as well as the a validation for using the Drude model in THz regime.

2.2.1 Optical properties of materials

In the Drude model, the free electrons gas of a metal, plasma, oscillate under an oscillating electric field E, and their motion is damped due to collisions with ions. All the other potentials such as, electron-electron interaction or electron-ion interaction are ignored except the potential of the applied electric field. The equation of motion for an individual electron of mass m can be described by

$$m\frac{\partial^2 x}{\partial t^2} + m\gamma\frac{\partial x}{\partial t} = -eE \tag{2.3}$$

For an electric field $\vec{E} = \vec{A}e^{-i\omega t}$, the position of the free electron is given by

$$\vec{x}(t) = \frac{e}{m(\omega^2 + i\gamma\omega)}\vec{E}(t) \tag{2.4}$$

where γ is the collision frequency and e is the charge of electron. Using Maxwell's equations, Eq 2.4 leads to the frequency dependent dielectric function $\epsilon(\omega)$ of metals given by

$$\epsilon(\omega) = 1 - \frac{\omega_p^2}{\omega^2 + i\gamma\omega} \tag{2.5}$$

where ω_p= $\sqrt{\frac{ne^2}{\epsilon_0 m}}$ is the plasma frequency. ϵ_0 is the permittivity of the free space. The dielectric function is a complex function where the real part is $\epsilon_r(w) = n^2 - \kappa^2$, and the imaginary part is $\epsilon_i(w) = 2n\kappa$. In the Drude model, the real and imaginary parts are given

Metal	$\omega_p[Hz]$	$\gamma[s^{-1}]$
Cu	1.12×10^{16}	1.38×10^{13}
Al	2.24×10^{16}	1.24×10^{14}
Au	1.37×10^{16}	4.05×10^{13}

Table 2.1: The plasma frequency ω_p and the collision frequency γ

by

$$\epsilon_r(\omega) = 1 - \frac{\omega_p^2 \tau^2}{1 + \omega^2 \tau^2} \tag{2.6}$$

$$\epsilon_i(\omega) = \frac{\omega_p^2 \tau}{\omega(1 + \omega^2 \tau^2)} \tag{2.7}$$

where n and κ are the real and the imaginary parts of the refractive index respectively and τ is the reciprocal of the collision frequency. It can be seen from Eq 2.6 that for frequencies less than the plasma frequencies $\omega < \omega_p$, ϵ_r is negative. In this region, metals show their metallic characteristics reflecting most of the incident light. For $\omega >> \gamma$, Eq 2.5 can be approximated to

$$\epsilon(\omega) = 1 - \frac{\omega_p^2}{\omega^2} \tag{2.8}$$

The plasma frequency for most metals is in the ultraviolet region (5). The plasma frequency and the collision frequency are shown in table for selected metals (15).

The AC conductivity derived from the of Drude σ model can be calculated using Ohms law $\vec{j} = -Ne\frac{\partial x}{\partial t} = \sigma \vec{E}$ given by

$$\sigma(\omega) = \frac{Ne^2\tau}{m} \frac{1}{1 - i\omega\tau} = \frac{\sigma_0}{1 - i\omega\tau} \tag{2.9}$$

where N is the density of the electron gas and σ_0 is the DC conductivity (7). For small frequencies $\omega << \gamma$, the distance where the amplitude of the electric field falls to $\frac{1}{e}$ of its original value on the surface is called the skin depth δ given by (16)

$$\delta = \sqrt{\frac{2}{\sigma_0 \mu_0 \omega}} \tag{2.10}$$

where μ_0 is the permeability of the free space; however, Eq 2.10 is not valid at THz frequencies as the collision frequency of metals is not much bigger than THz frequencies as illustrated in Table 2.2.1. A more accurate relation is presented for the skin depth at THz frequencies in the next sections.

2.2.2 Limitation of Drude Model

The conflict between the classical Drude model and experiment takes place when $\omega > \omega_p$ which is in the ultraviolet region. According to the Drude model, metals are transparent in this regime; however, they appear as different colors such as the reddish color of copper due to interband transitions. As this work is at the THz frequencies, the Drude model is valid in this regime (7).

2.3 Surface Plasmon Polaritons

Solving Maxwell's equations for a TM [1] wave that propagates parallel to the surface of metal-dielectric interface leads to the dispersion relation that is the wave vector in the propagating direction given by

$$\beta = k_0 \sqrt{\frac{\epsilon_m \epsilon_d}{\epsilon_m + \epsilon_d}} \tag{2.11}$$

where $k_0 = \frac{\omega}{c}$ is the wave vector of the free space. ϵ_m and ϵ_d are the dielectric functions of the metal and dielectric respectively. The dispersion relation of the metal-dielectric interface is plotted versus the angular frequency in Figure 2.6. The curve on the left of the dispersion relation shows the radiative mode of metals where they become transparent for

[1] TM polarized light is a transverse magnetic polarized light where the magnetic field of the wave is parallel to the surface and the electric filed is perpendicular to the surface (7).

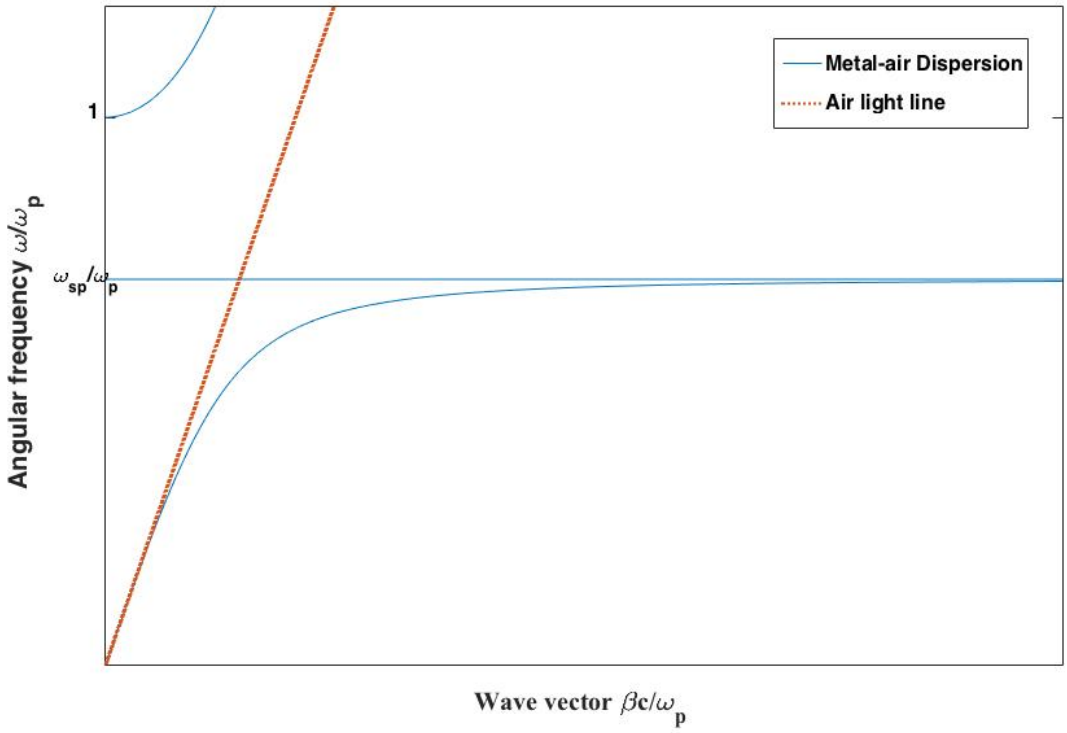

Figure 2.6: Dispersion relation of a metal-dielectric interface.

$\omega > \omega_p$. Below ω_p, metals become reflective and retain their metallic behavior, at these frequencies, the wave can be coupled into the surface of the metal-dielectric as a surface plasmon polariton (SPP). The dispersion curve of SPPs appears as the right curve of the dispersion relation in Figure 2.6. As β goes to infinity, the frequency known as the surface plasmon frequency ω_{sp} is given by

$$\omega_{sp} = \frac{\omega_p}{\sqrt{1+\epsilon_d}} \tag{2.12}$$

At this frequency, $\epsilon_m = -\epsilon_d$ and the wave decays exponentially in the normal direction to the surface. It can be seen from Figure 2.6 that the light line of the dielectric does not intersect with the SPPs at any frequency. Thus, the excitation of SPPs requires special techniques in order to couple the incident wave to the SPPs frequency. This momentum

matching can be achieved by several ways, such as prism coupling, grating coupling, and the excitation using highly focused optical beams. As seen from Eq 2.12, the excitation of SPPs can be achieved for frequencies close to ω_p of metals lying in optical and near-infrared frequencies (5).

The skin depth relation at THz frequencies can be derived using the solution of metal-dielectric interface problem mentioned in the beginning of this section. The wave vector in the normal direction to the surface is given by

$$k_z = k_0 \sqrt{\frac{\epsilon_m^2}{\epsilon_m + \epsilon_d}} \tag{2.13}$$

At THz frequencies, $\epsilon_m >> \epsilon_d$,hence, k_z can be approximated to

$$k_z = k_0 \sqrt{\epsilon_m} \tag{2.14}$$

The skin depth is $\frac{1}{k_z}$. As the imaginary part only is responsible for the exponential decay of the electric field in the z direction, the skin depth is given by (17)

$$\delta = \frac{1}{Im(k_z)} = k_0 \frac{1}{\sqrt{\epsilon_m}} \tag{2.15}$$

The skin depth calculated by Eq 2.15 of copper at 1 THz is about $0.16\,\mu\mathrm{m}$ while it is $1.7 \times 10^{-6}\,\mu\mathrm{m}$ when Eq 2.10 is used.

2.4 Extraordinary Optical Transmission (EOT)

In 1998, the transmission of light through a subwavelength hole array in a silver thin film known as extraordinary optical transmission (EOT) was first seen by Ebbsene and his colleagues. The transmission was attributed to the excitation of SPPs on the metal surface (8). The periodicity of apertures increases the momentum of the incident wave in both directions in the surface enabling the momentum matching condition between the incident light

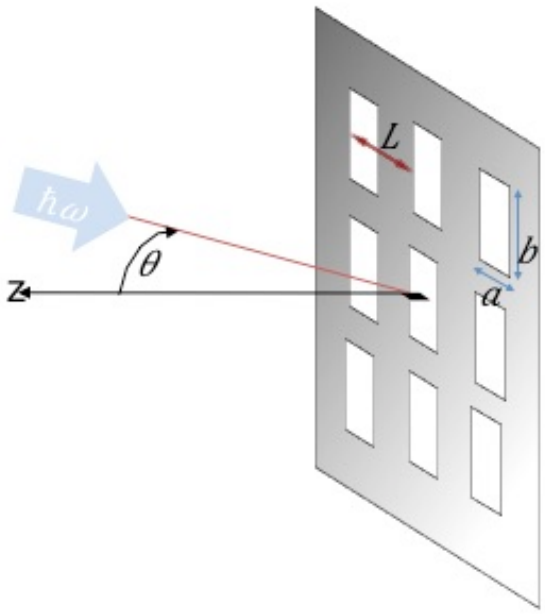

Figure 2.7: An incident wave with angle θ on an array of apertures of periodicity length L and rectangular apertures of width a and length b arranged in a square lattice.

and the SPPs dispersion. For an incident wave at an angle theta from the surface normal, as seen in Figure 2.7, the momentum matching condition is given by (3)

$$\vec{\beta} = k_0 sin\theta\vec{i} \pm n\vec{G_x} \pm m\vec{G_y} \tag{2.16}$$

where $\vec{G_x}$ and $\vec{G_y}$ are the reciprocal lattice vectors. n and m are integers. For normal incidence in a square lattice Eq 2.16 becomes

$$|\vec{\beta}| = \sqrt{n^2 + m^2}\frac{2\pi}{L} \tag{2.17}$$

where $|\vec{G_x}|$ and $|\vec{G_y}| = \frac{2\pi}{L}$ for a square lattice and L is the array periodicity length. Using Eq 2.11 in Eq 2.17 and solving for the wavelengths of where the SPPs take place, the wavelength of the SPPs is given by (3)

$$\lambda_{sp} = L\frac{1}{\sqrt{n^2 + m^2}}\sqrt{\frac{\epsilon_m\epsilon_d}{\epsilon_m + \epsilon_d}} \tag{2.18}$$

When the transmitted light becomes tangential to the array's plane, the diffracted light leads to minima resonance called Wood's anomalies. The wavelength of theses antiresonance transmission that are slightly shifted from the resonant frequency is given by (18)

$$\lambda_{wood} = L\frac{1}{\sqrt{n^2+m^2}}\sqrt{\epsilon_d} \tag{2.19}$$

At THz frequencies, $\sqrt{\frac{\epsilon_m\epsilon_d}{\epsilon_m+\epsilon_d}}$ can be approximated to $\sqrt{\epsilon_d}$ as seen from Figure 2.9. The maximum SPPs wavelength λ_{peak} can be simplified to (4)

$$\lambda_{peak} = L\sqrt{\epsilon_d} \tag{2.20}$$

where $n^2 + m^2 = 1$

It can be seen from Eq 2.18 that L plays a significant role in achieving the momentum matching in a wide range of frequencies to excite the SPPs. When SPPs are initiated, it propagates on the surface while part of the wave tunnels through the apertures. The SPPs dispersion curve for an incident wave with an angle θ on a free-standing metal is plotted in Figure 2.8. The intersections of SPPs dispersion curve with the incident light represent the coupling frequencies of the SPPs (19).

2.4.1 Time of Flight Model

Although there is no unified theory that describes the EOT phenomenon, THz time domain spectroscopy has lead to a better understanding of how EOT works. Investigating the role of different factors that shift or broden the resonant frequency of the EOT is essential in order to engineer EOT devices for applications. The time of flight model is a qualitative model that was enhanced by the observations of the THz temporal waveform. This model is presented particularly as the only model that explained the effects of changing the shape, dimensions, area, aspect ratio and the polarization direction on the resonant frequency. Although the effect of changing the thickness of the EOT device is not included in the

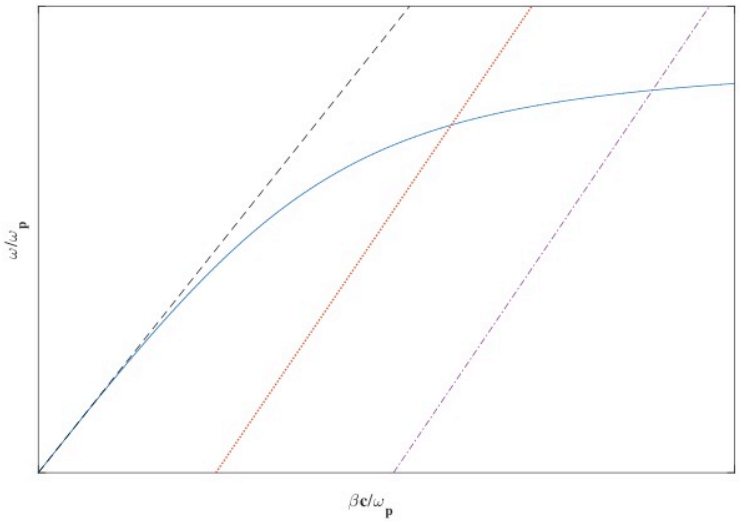

Figure 2.8: The dispersion relation of a free-standing EOT device. The dotted line on the left is the light line. The curve is the SPPs dispersion curve intersected with two incident light shifted to the right from the light line due to the gained momentum in the two dimension array. The two shifted lines are for different frequency orders that have different m and n.

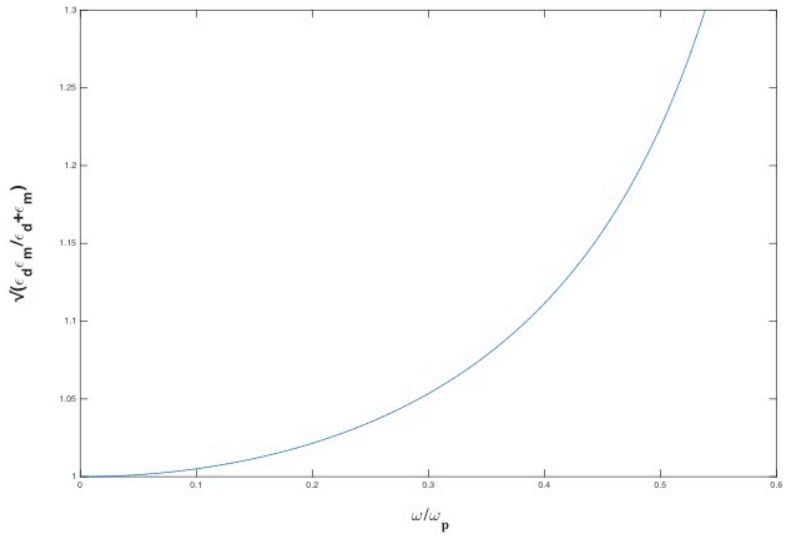

Figure 2.9: The quantity $\sqrt{\frac{\epsilon_m \epsilon_d}{\epsilon_m + \epsilon_d}}$ can be approximated to $\sqrt{\epsilon_d}$ at THz frequencies. For metal-air EOT device $\sqrt{\frac{\epsilon_m \epsilon_d}{\epsilon_m + \epsilon_d}}$ approaches 1, air dielectric constant, as $\frac{\omega}{\omega_p}$ approaches THz frequencies.

time of flight model, it is covered in literature as it is presented in the next section. The underlying assumption in the time of flight model is that the time in a half cycle seen in the time domain is the decoupling time of SPPs given by

$$t_{TOF} = \frac{L - a}{v_{spp}} \tag{2.21}$$

where v_{spp} is the SPPs velocity. The resonant frequency in the time of flight model is associated with the decoupling time not the plasma frequency. The positive cycle of the incident polarized THz wave couples to SPPs on the surface, propagates, and decouples into the free space through the apertures. The second negative cycle couples to SPPs later on time on the surface, propagates in the opposite direction, and decouples into the free space through the apertures. The successive coupling and decoupling events of both the positive and negative parts of the THz beam appear as a periodic cycles in the time domain. The time domain and frequency domain transmission through a copper-based EOT device can be seen from Figure 2.10. The periodic cycles decay in time as the SPPs are lost due to both coupling and decoupling events. Increasing the width of the aperture decreases the metallic regions between the apertures which reduces the decoupling time. This can be seen as an increase in the number of oscillations in the time domain transmission measurements leading to a blueshift of the resonant frequency in the frequency domain. Increasing the width too much causes the next nearest neighbor event instead of the nearest event leading to a broadening in the resonant frequency due to the mix of the nearest and next nearest neighbor event. As the aspect ratio is kept constant, increasing the length causes redshift and broadening as well. It can be seen from the previous description that the polarization is preferred to be perpendicular to the long side. As it is perpendicular to the short side, it is more likely to get the next nearest neighbor event due to the narrow regions in the direction of propagation leading to broadening in the resonant frequency. The transmission of light through the apertures increases with increasing the area; however, it is affected by changing the width and length as described before due to changing the area (4). The nearest and next

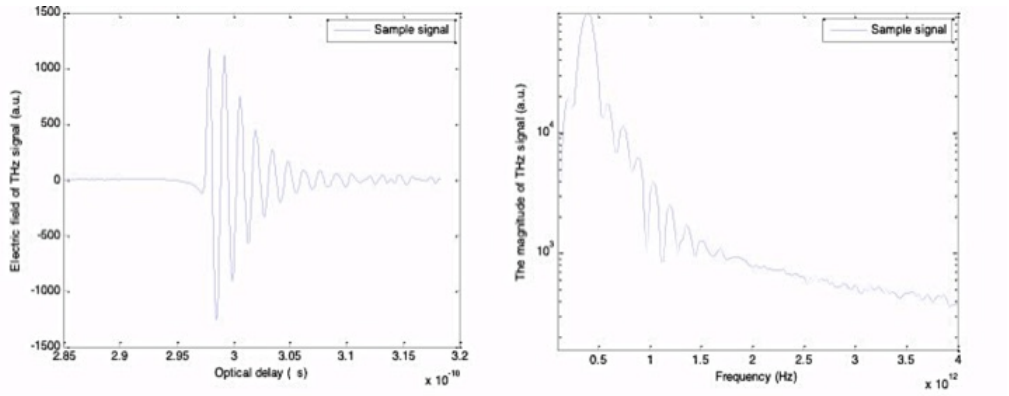

Figure 2.10: The time domain (on the left) and the frequency domain of transmission measurements (on the right) of copper-based EOT device.

nearest neighbor events are described in Figure 2.11

2.4.2 Thickness of an EOT device

The role of changing the thickness of the EOT device is reported theoretically and experimentally at optical and THz frequencies for different metals in the literature. In the optical regime, the SPPs of thin samples couple from both sides of the thin film resulting in an increase of the resonant frequency while the coupling of the SPPs from both sides does not happen for thicker samples, and the transmission decays exponentially with increasing the thickness (20). This was reported experimentally for Ag EOT devices where the transition between the two behaviors took place for a thickness equal to three times the skin depth. The transition thickness was observed from the transition peak that was increasing for thicknesses less than the transition thickness reaching its maximum value at the transition thickness followed by a decrease in the transmission peak (21). The exponential decay of increasing the thickness was reported as well for THz frequencies for a n-type silicon EOT device (22). Other THz research examined the transmission below and above the skin depth. It was shown that for lead with a skin depth of 320 nm, SPPs started to be seen at 64 nm; however, around 76% of the transmission peak efficiency, normalized to the transmission peak of the skin depth, occurred at one third of the skin depth called the

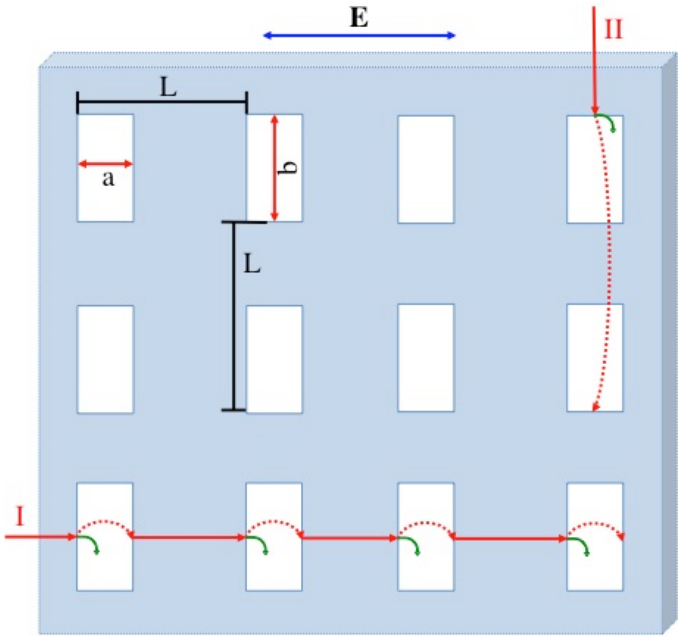

Figure 2.11: The coupling (continuous red line) and decoupling (green line) of the incident polarized wave I perpendicular to the long side of the apertures represent the nearest event while the coupling and recoupling of the incident wave II perpendicular to the short side of the apertures represent the next nearest neighbor event. The direction of the electric field points to the preferred direction normal to the long side.

critical thickness. Below the critical thickness, the transmission peak increased exponentially until it reached the critical thickness above which it was saturated until it reaches its maximum value at the skin depth (17). Additionally, at THz frequencies, it was shown that Al had negligible resonant transmission below $\frac{\delta}{15}$ where δ is the skin depth. After that, the transmission peak started to increase until it reached the skin depth with a slight increase followed the increase of the thickness above the skin depth (23).

2.4.3 EOT of Carbon Nanotubes

Studies of EOT of carbon nanotubes (CNT) thin films is limited in literature where two out of three studies reported EOT from the fabricated CNT thin films. The tunability of the CNT is an advantageous point in exploiting EOT devices for applications. All samples in literature were fabricated using the same technique. Nguyen's work in (10) is presented in detail as its sample is used for the basis of the simulation part. The free standing CNT thin film was drawn from a side wall of a forest of multi-walled CNT (MWCNT) that was synthesized using catalic chemical vapor and deposited on a steel washer. The thickness was increased by stacking the thin films together parallel to each other providing 25 micron and 60 micron thick samples. The array of circular holes were drilled by an excimer laser. Using THz time domain spectroscopy, the thinner sample showed resonant transmission in the frequency domain when the alignment of the CNT is parallel to the polarization direction of the THz wave while no resonance was observed when the polarization is perpendicular to the alignment of the CNT. The resonant transmission was not observed for the thicker sample in both alignments of the CNT. The optical properties of the 25 micron thick sample were calculated using time domain spectroscopy (10). The results were extracted from the paper and plotted in Figure 2.12.

The other study that reported resonantly enhanced transmission were for 3 micron thick CNT thin film of rectangular array of apertures. The resonance was seen for the parallel orientation of the CNT with the polarization of the incident light as well (9). In this study,

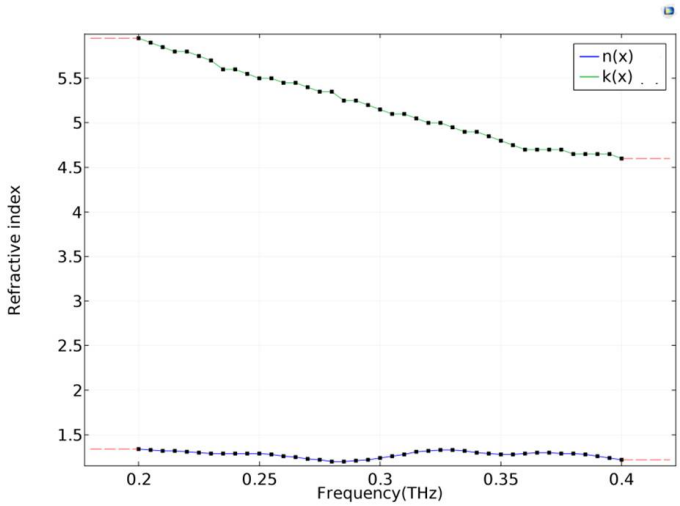

Figure 2.12: The real part (blue) and the imaginary part (green) of the refractive index as it is extracted from (10).

Woods anomalies were seen as a minimum transmission in the frequency domain. The 1 micron and 3 micron of 50 micron aquare holes showed a broadened resonant transmission (9).

Chapter 3

Modeling of the EOT Device

The simulation part of this work is implemented using the Finite Element Method (FEM). The procedure of modeling a physics problem using FEM requires four basic steps starting from defining the modeling domain and sub-domains that are divided into discrete number of elements followed by setting up the governing approximated partial differential equations of the physical system. The system can be solved numerically after defining the boundary conditions that retain the continuity of the solution and the initial conditions for each element in the domain constructing the global matrix coefficients (24). The discrete number of elements in the domain represents the mesh of the modeled system. These elements could be defined as shapes such as rectangular or triangular in the 2D simulations or blocks or tetrahedral for 3D simulations. Commercial software such as, ANSYS, ANSOT, and COMSOL Multiphysics that have Graphical User Interfaces has expanded using FEM in broad applications (25). This work is performed using the COMSOL Multiphysics RF module. As the RF module software is specialized for Microwave and Radio frequency designs, modeling THz frequencies is possible as well. The simulation in this module is based on solving Maxwell's equations with many features that enable one to choose the solution type, built-in materials, and various boundary conditions that meet the simulation

demands (26).

3.1 Modeling Technique

In order to study both copper and CNT EOT devices, a polarized THz wave is excited in a hypothetical air waveguide by defining one port in front of the sample while the other port is defined behind the sample to verify the resonance of the transmitted wave using S-21 parameter calculations. S-parameters are scattering scalar complex values that indicate how much energy is transmitted or reflected. For two ports, the power wave coefficients a_1, b_1, a_2, b_2 are related to the S-parameter by

$$\begin{pmatrix} b_1 \\ b_2 \end{pmatrix} = \begin{pmatrix} S_{11} & S_{12} \\ S_{21} & S_{22} \end{pmatrix} \begin{pmatrix} a_1 \\ a_2 \end{pmatrix} \tag{3.1}$$

where a_1 is the incident power wave on port 1, b_1 is the reflected power wave on port 1, a_2 is the incident power wave on port 2, b_2 is the reflected power wave on port 2 (27). The power wave parameter are demonstrated in Figure 3.1. As only one port is excited in our simulation, the S_{21}-parameter is given by

$$S_{21} = \frac{b_2}{a_1} \tag{3.2}$$

In general, S-parameters are complicated values; however, the S_{21}-parameter can be described generally as

$$S_{21} = \sqrt{\frac{power\ delivered\ to\ port\ 2}{power\ incident\ on\ port\ 1}} \tag{3.3}$$

and the time average power transmission coefficient is $|S_{21}|^2$ (28). Consequently, the magnitude of S_{21}- parameter represents the transmission coefficient as used in the simulation. The modeling methodology is divided into 3 sections describing the geometry, materials, and boundary conditions.

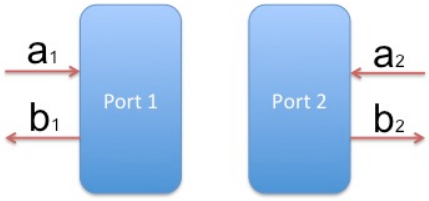

Figure 3.1: The power wave parameters. a_1 is the incident power wave on port 1, b_1 is the reflected power wave on port 1, a_2 is the incident power wave on port 2, b_2 is the reflected power wave on port 2.

3.1.1 Geometry

The geometry of the array of the EOT device plays an important role in determining the resonant frequency as described in Eq 2.20. The geometry of the copper-based EOT device that has a 50 micron thickness was selected to yield enhanced transmission at 0.96 THz as $L = 312.5\,\mu\mathrm{m}$. Based on the time of flight model, the polarization direction was selected to be normal to the long side in order to avoid the next nearest neighbor event which leads to a broadened transmission. The width, length, and area of the aperture were chosen from (4) where they showed the best enhancement experimentally. The rectangular apertures are arranged in a triangular lattice with width of $40\,\mu\mathrm{m}$ and length of $160\,\mu\mathrm{m}$ as it can be seen from Figure 3.2 for a unit cell of the copper device. The geometry of the CNT-based EOT device that has a 25 micron thickness in (10) is used in the simulation as it showed a resonant transmission experimentally. This device has a calculated resonance at 0.25 THz as $L = 1.2\ mm$. The circular apertures of a diameter = 0.65 mm are arranged in a square lattice as it can be seen from Figure 3.3.

3.1.2 Materials

For the copper-based EOT, the material is defined as copper using COMSOL's built-in library while the electrical properties of the CNT thin film were extracted from experimental data from Wang et. al (10). In our model, the dielectric constant is defined as a function of the frequency dependent refractive index. The frequency dependent conductivity Drude

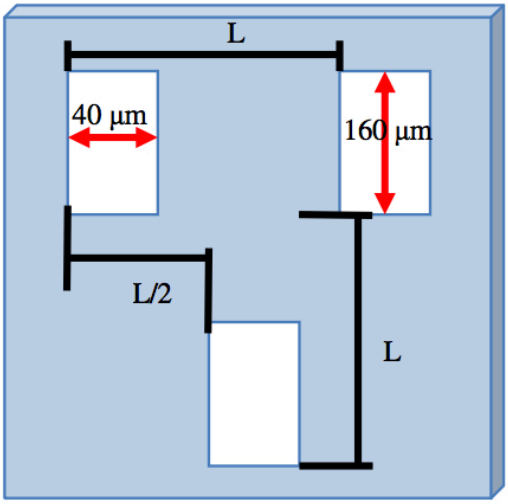

Figure 3.2: The aperture dimensions and lattice arrangement of a unit cell of the copper-based EOT device of $50\,\mu\mathrm{m}$ thickness and peridicity length $L = 300\,\mu\mathrm{m}$. The rectangular apertures arranged in a triangular lattice have width of $40\,\mu\mathrm{m}$ and the length of $160\,\mu\mathrm{m}$.

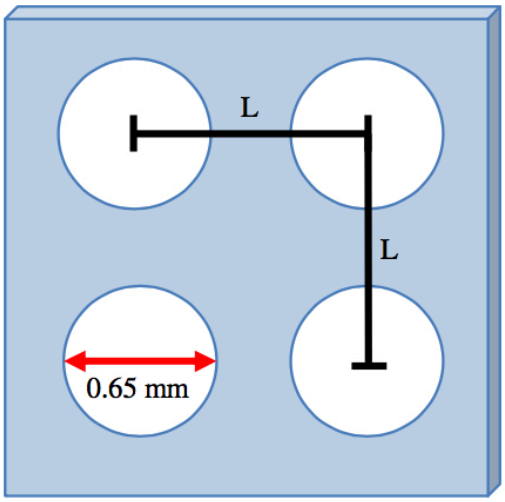

Figure 3.3: The aperture dimensions and lattice arrangement of a unit cell of the CNT-based EOT device of $25\,\mu\mathrm{m}$ thickness and peridicity length L=1.2 mm. The circular apertures arranged in a square lattice have a diameter= 0.65 mm.

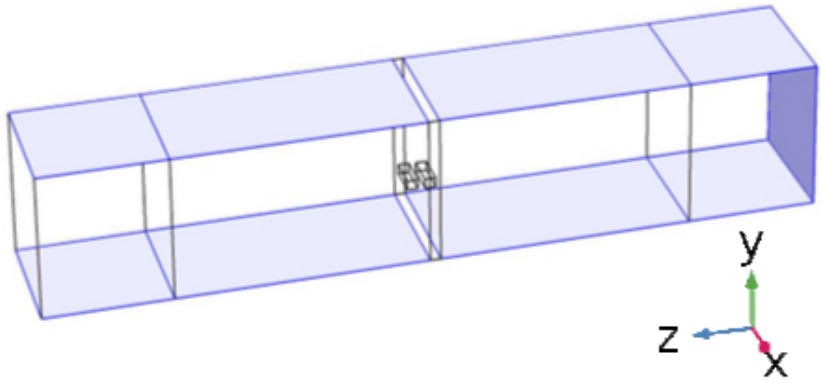

Figure 3.4: The PEC boundaries are chosen to be normal to the electric field polarization direction (along y) while the other sides are defined to be PMCs. This configuration yields an infinite plane wave and infinite periodic array.

model in Eq 2.9 is used to define the conductivity of the device.

3.1.3 Boundary Conditions

The THz wave propagates in a hypothetical air-filled waveguide that is set with perfect electric conductors (PEC) on the sides normal to the polarization direction while the other sides are set as perfect magnetic conductors (PMC). This particular configuration allows one to excite an infinite plane wave in the x and y directions propagating in the z direction which models an infinite periodic array Figure 3.4.

Due to the low penetration of the THz wave in copper and CNT materials (values calculated from the skin depth of both devices as described in Eq 2.15, the outer faces of the EOT device are set with the impedance boundary condition (IBC). As the penetration is very low in the metal, Maxwell's equation are solved on the surfaces of the metal that are defined as IBC instead of including the whole interior domain that requires a huge mesh density as each element should be less than the skin depth consuming a lot of memory (29). The ohmic losses are taken into account too in the IBC where it is still accurate for

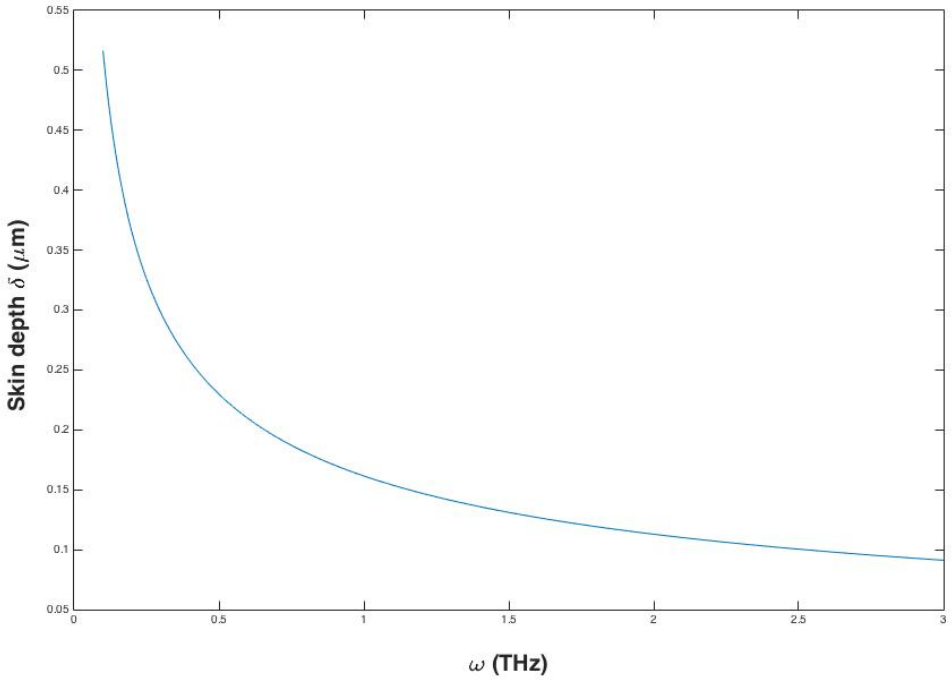

Figure 3.5: The skin depth of copper from 100 GHz to 3 THz. The skin depth has 1×10^{-7} order of magnitude at THz frequencies.

thicknesses bigger than ten times the skin depth (29). The skin depth is plotted versus the frequency range in the simulation of copper in Figure 3.5. The boundaries at the end of the air waveguide along the propagation direction are defined as perfectly matched layers (PML) in order to minimize the undesired reflections.

For solving electromagnetic problems using FEM, the mesh element size must be half of the wavelength or smaller. Meshing of both devices is defined by a Physics Controlled Mesh with maximum element size equal to $\frac{\lambda}{6}$ leading to higher accuracy. The maximum element size of the IBC boundaries is defined to be less than the skin depth of both materials. The mesh of the copper device model is shown in Figure 3.6.

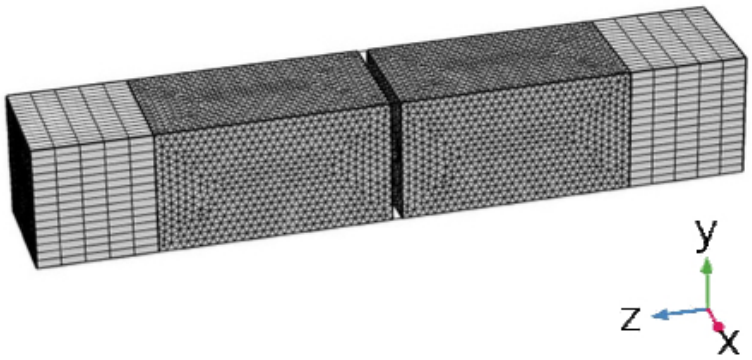

Figure 3.6: Meshing of both devices is defined by a physics controlled mesh with maximum element size equal to $\frac{\lambda}{6}$. The maximum element size of the IBC boundaries is defined to be less than the skin depth of both materials.

3.2 Analysis of the modeled EOT Device

3.2.1 Transmission Results

The copper-based EOT device that has a calculated resonance at 0.96 THz exhibits a red-shifted resonant transmission frequency at 0.86 THz (Figure 3.7). Experimentally, a copper-based EOT device which has similar aperture dimensions and L= 300 mm associated with a theoretical resonance at 1 THz showed a red-shifted resonance as well at 0.85 THz (4). The low transmission at 0.6 THz and at the resonant frequency are shown in Figure 3.8 (a) and (b). A Wood's anomaly of the destructive interferences is seen experimentally at 1.14 THz (4) and at 1 THz in the model. The surface wave that confirms the EOT is seen on the surface of the copper device as in Figure 3.9 (a).

The S_{21}-parameter calculations of a CNT- based EOT device (Figure 3.10) shows a very sharp resonance at 0.235 THz followed by a dip at 0.25 THz that corresponds to Wood's anomaly and it starts increasing again until 0.35 THz followed by another dip. According to the designed CNT- based device, the resonant frequency is in good agreement with

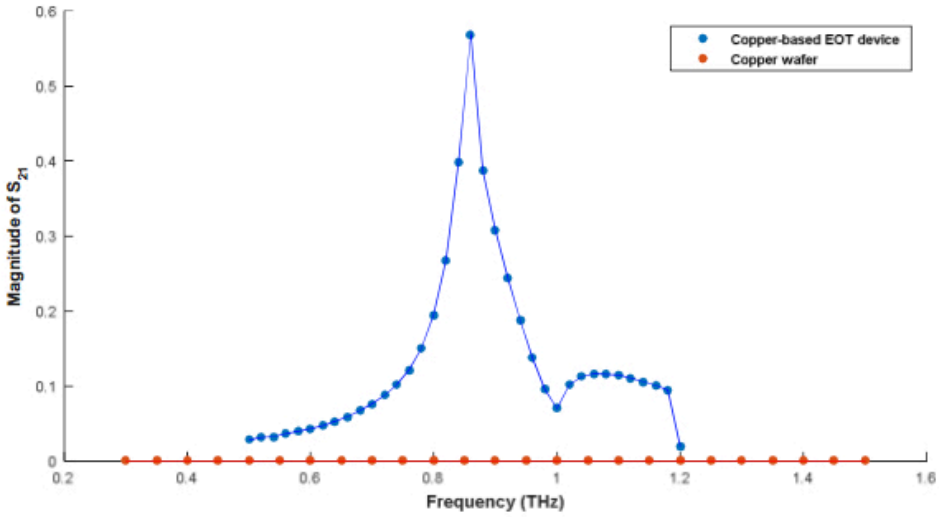

Figure 3.7: The magnitude of the S21-parameter of the copper-based EOT device exhibits a resonant frequency at 0.86 THz. The red line shows the low transmission through a copper wafer.

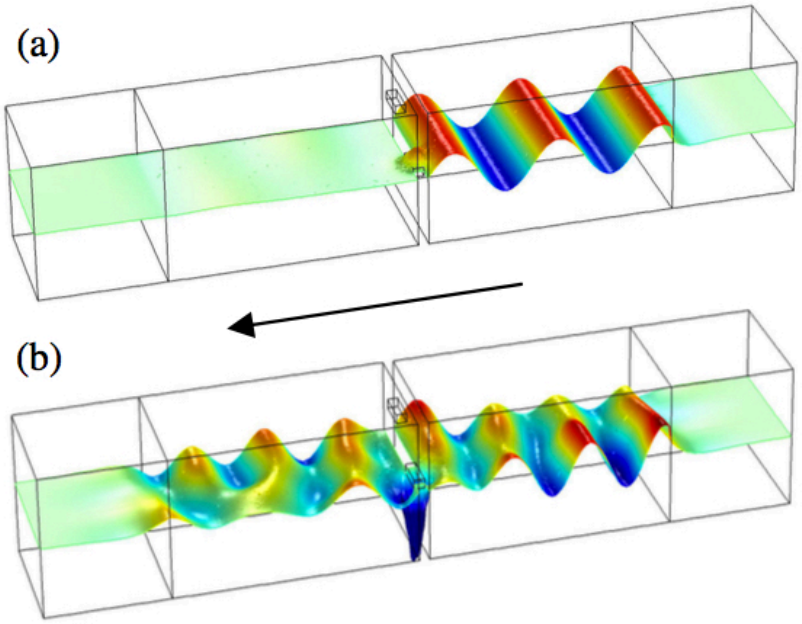

Figure 3.8: The transmitted wave through the copper-based EOT device at (a) 0.6 THz (b) the resonant frequency 0.86 THz. The wave is propagating from right to left.

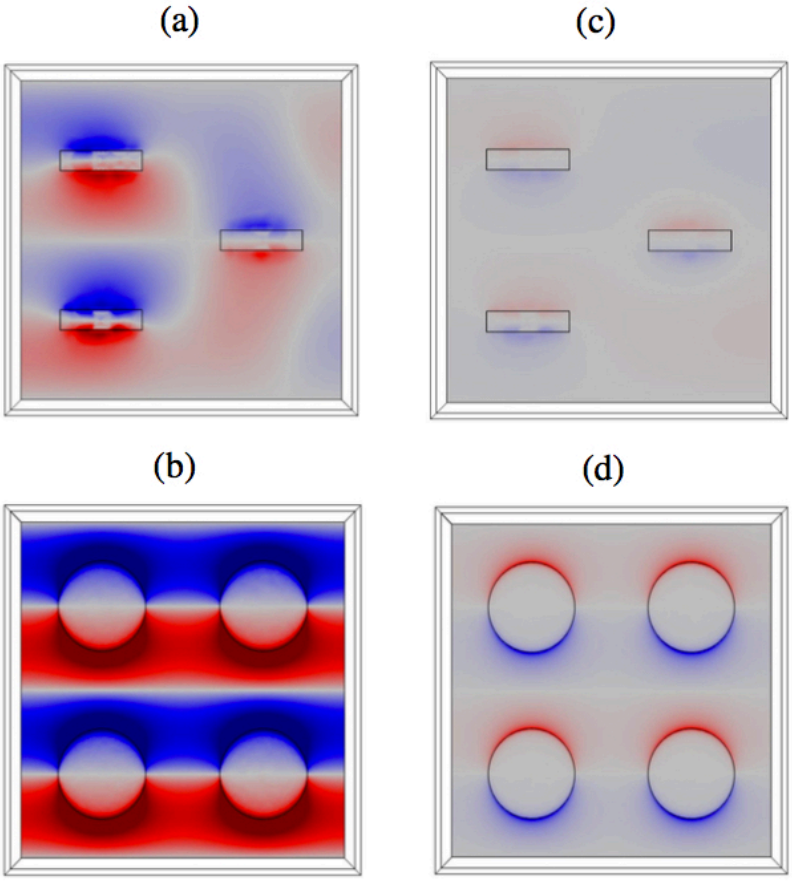

Figure 3.9: The z-component of the electric field on the surface (xy plane) at (a) 0.86 THz of the copper-based EOT device (b) 0.235 THz of the CNT-based EOT device shows the coupling and propagating of the wave on the surface. The propagation of the surface wave cannot be seen at a lower frequency (c) 0.60 THz of the copper-based EOT device (d) 0.1 THz of the CNT-based EOT device. The intensity scale is the same for both images, and the same wave appears in both sides of the EOT device.

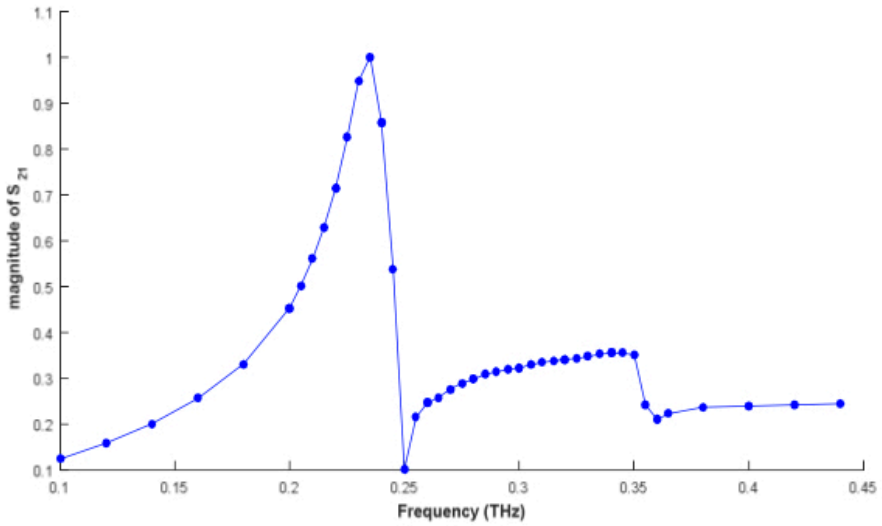

Figure 3.10: The magnitude of the S21-parameter of the CNT-based EOT device exhibits a resonant frequency at 0.235 THz.

the experiment (10) where both of them are slightly shifted from the first order calculated resonance from Eq 2.18 located at 0.25 and corresponded to $(0, \pm 1)$ or $(\pm 1, 0)$. Woods anomalies and the second order of the resonant frequency corresponded to $(\pm 1, \pm 1)$ and calculated to be at 0.354 THz are seen in our model only. The coupling and recoupling of the z- component of the electric field on the surface of CNT device are seen as in Figure 3.9 (b) and (d). In order to verify whether we have a mesh dependent result, finer meshes have been tested and showed no difference. The polarization dependency with the orientation of the CNT is verified as there is no transmission seen for the polarization direction perpendicular to the CNT EOT device. Additionally, there is no difference observed in the transmission as the real and imaginary parts of the refractive index are changed up to 100% of their original values which verifies that the EOT transmission is not affected by the metal properties as given in Eq 2.20.

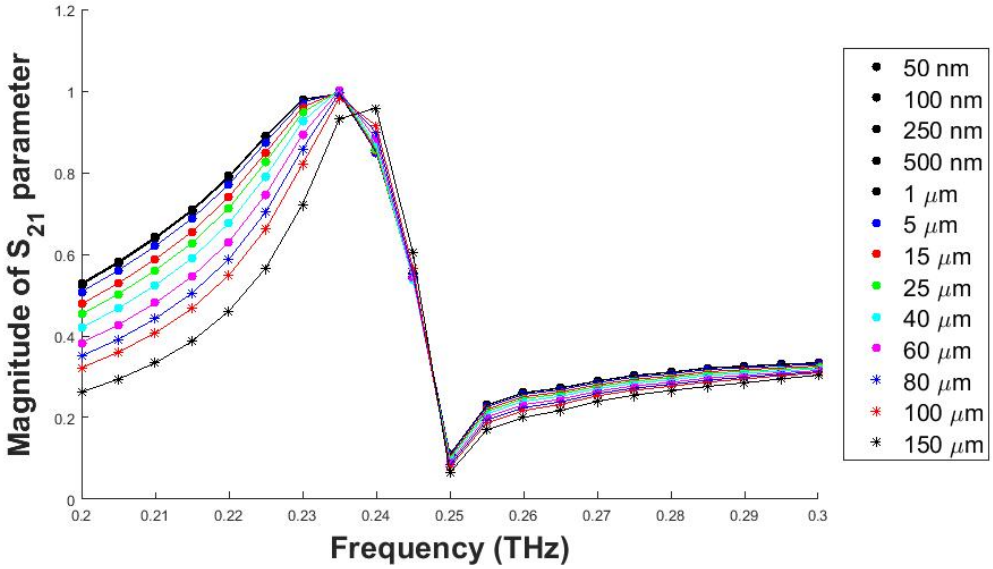

Figure 3.11: The transmission of the CNT EOT device of multiple thicknesses ranging from 50 nm to $150\,\mu\mathrm{m}$.

3.2.2 Transmission as a Function of Thickness

The transmission of the CNT EOT device is shown in Figure 3.11 for different thicknesses ranging from 50 nm to $150\,\mu\mathrm{m}$. The results are presented in a 3D graph as shown in Figure 3.12. From 50 nm to $1\,\mu\mathrm{m}$ the transmission is nearly the same while it shows an interesting behavior from $1\,\mu\mathrm{m}$ to $150\,\mu\mathrm{m}$ that can be divided into three basic regions, pre-resonance region from 200 GHz to 220 GHz, near resonance region from 225 GHz to 230 GHz, post-resonance region from 250 to 300 starting from Wood's anomaly at 250 GHz. Although all regions fall exponentially with increasing the thickness as it is reported experimentally and theoretically in (17; 20; 21; 22), the pre-resonance region appears to fall rapidly in comparison to the near resonance region.

Figure 3.13 shows the exponential decay with increasing thickness for selected frequencies in each region. As the simulation results are fitted to an exponential decay, this observation can be further clarified by plotting the decay coefficient α versus the frequency as in Figure 3.14. As the frequency increases, α falls to its minimum value in the near res-

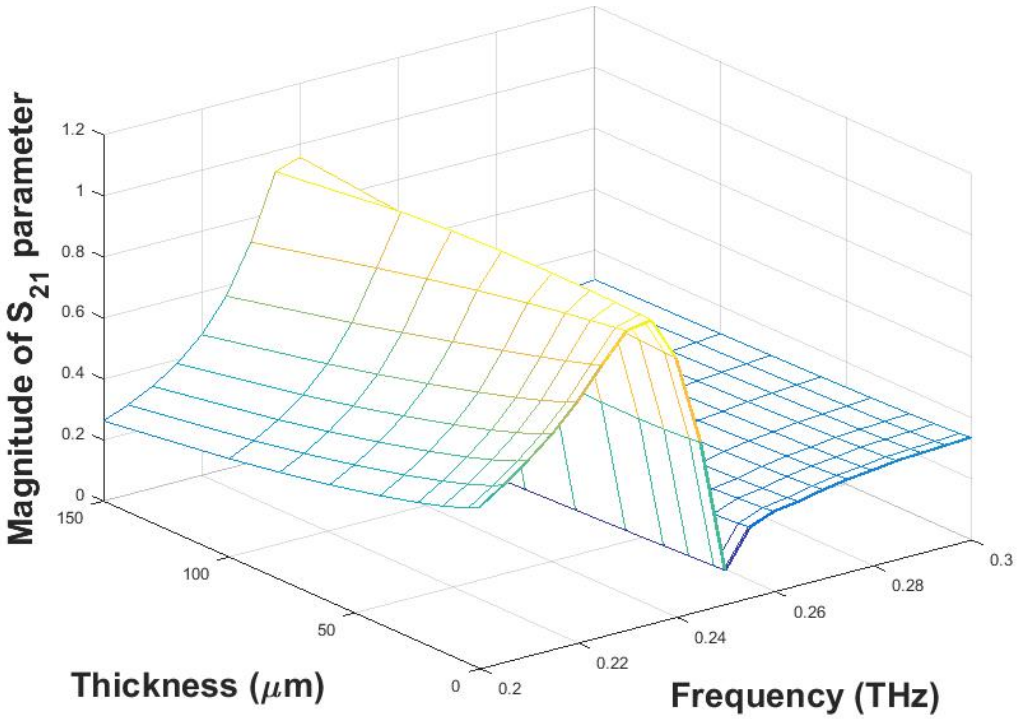

Figure 3.12: 3D graph of the transmission of the CNT EOT device of multiple thicknesses ranging from 50 nm to $150\,\mu\mathrm{m}$ and frequencies from 200 GHz to 300 GHz.

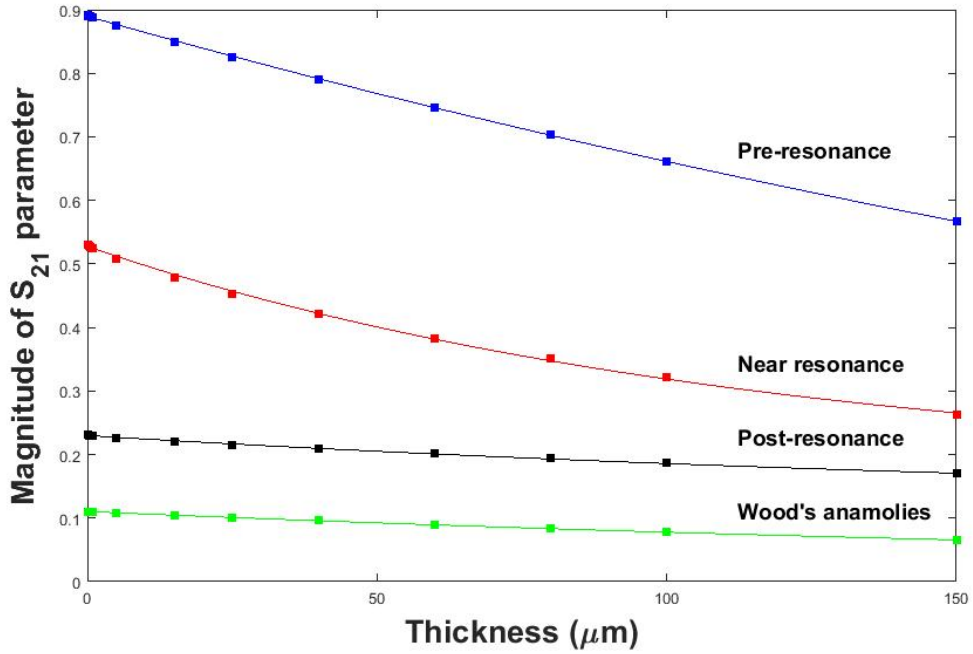

Figure 3.13: The transmission falls exponentially eith increasing the thickness for all three regions, pre resonance at 200 GHz, near resonance at 225 GHz, and post resonance at 255 THz. The exponential decay of wood's anamoly at 250 GHz is shown.

onance region at 230 GHz confirming the EOT phenomenon as the transmission is higher close to the resonant frequency. The dip is followed by an increase in the decay coefficient as the frequency increases in the post-resonance region. The exponential attenuation has its maximum value as the frequency exceeds 275 GHz.

At resonance, it can be seen from Figure 3.11 that the transmission peak is blue-shifted with increasing the thickness. The behavior of the transmission peak is consistent with the experiment in (17; 23) that the transmission peak increases with increasing the thickness reaching its maximum value at the skin depth as seen from Figure 3.15. The skin depth of the CNT EOT at the resonant frequency is $36.3\,\mu\mathrm{m}$ calculated from Eq 2.15. The maximum peak that appears at $40\,\mu\mathrm{m}$ shows good agreement. Experimentally, the transmission peak stayed constant approximately with increasing the thickness (17; 23) reaching 2δ. In our model, the transmission peak started to decrease after the skin depth until the maximum thickness in the simulation which is 4δ. The results of the transmission peak are fitted to a

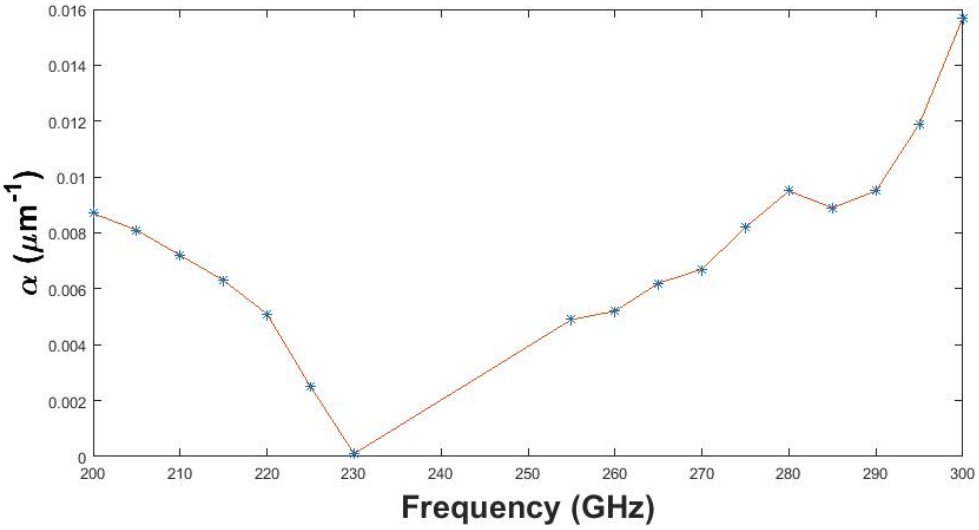

Figure 3.14: The decay coefficient α of the transmission as a function of the frequencies in pre-resonance, near resonance, and post-resonance regions.

quadratic polynomial in order to calculate the critical thickness that is the maximum thickness where the resonantly enhanced transmission can no longer be seen. The calculated critical thickness is about $448\,\mu\mathrm{m}$ as in Figure 3.16. The transmission at the frequency 240 GHz followed the resonance directly shows a minimum transmission at the skin septh as shown in Figure 3.17

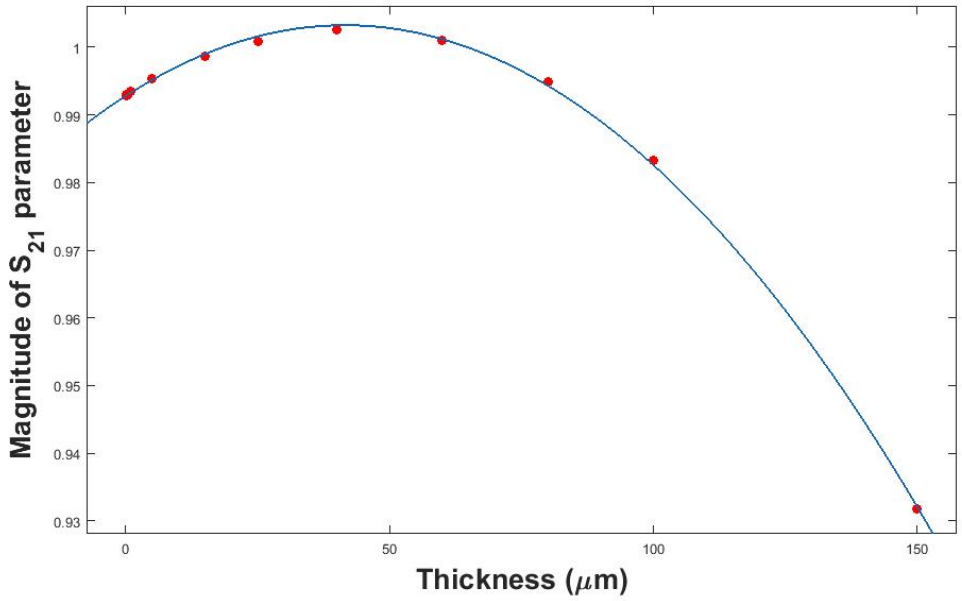

Figure 3.15: The transmission peak as a function of the thickness has its maximum value at $40\,\mu\mathrm{m}$ close to the calculated skin depth. The simulation data is fitted to quadratic function.

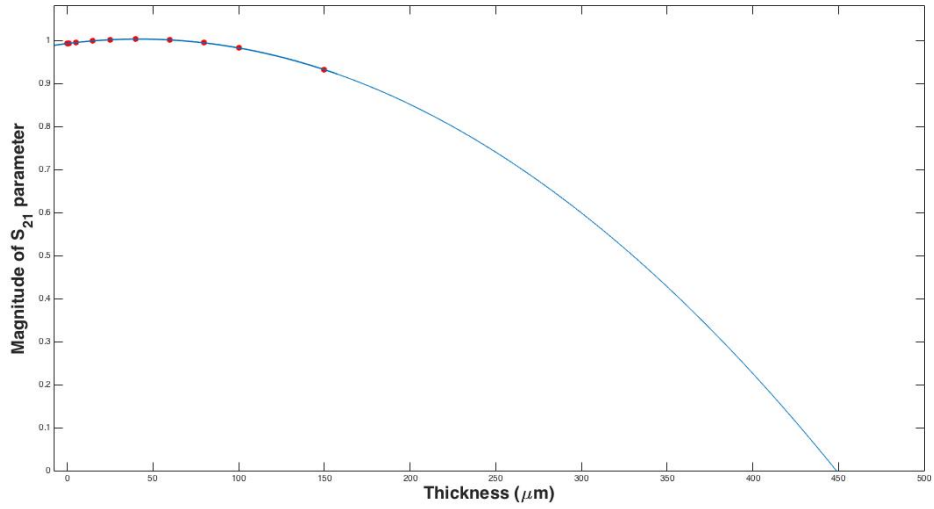

Figure 3.16: The critical thickness where the resonantly enhanced transmission can no longer be seen appears at $448\,\mu\mathrm{m}$ calculated from the fitting results.

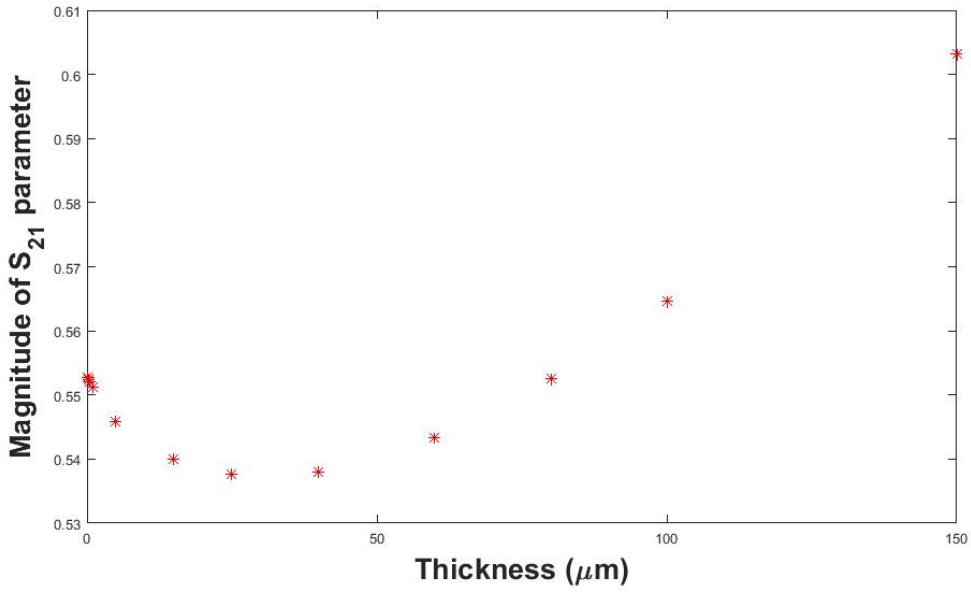

Figure 3.17: The transmission at the frequency 240 GHz followed the resonance directly shows a minimum transmission at the skin septh $40\,\mu\mathrm{m}$.

Chapter 4

CNT EOT Device

4.1 CNT-based EOT Device Fabrication Process

This chapter describes efforts involving the design, fabrication, and characterization of an EOT CNT device. The experiment is designed to investigate the impact of the other factors other than the thickness, such as aperture shape, lattice arrangement, and area by utilizing a different fabrication method of the CNT aligned thin films than reported in literature. Using the samples illustrated in Figure 4.1, effects on transmission due to changing the apertures shape (symmetric and asymmetric), lattice arrangement (square and triangular), and periodicity length can be investigated. The impact of changing the periodicity length is added to confirm the linear relation between L and the resonant wavelength for CNT at THz frequencies. The 9 samples are grouped in 3 sets, first set of samples 1-3, second set from 4-6, and the third set from 7-9. Samples 1-6 have the same periodicity length corresponded to the same resonant frequency at 300 GHz for the CNT-air interface. The first set has a circular aperture that is arranged in a square a lattice arrangement except for sample 2 which has a triangular lattice. The area of the first two samples of the first set are kept the same while the area of the third sample is about 50% bigger than the other

samples of the same set. In the second set, all samples have rectangular apertures arranged in a square lattice except the second one of the same set that arranged in a triangular lattice. In this set, the area of the third sample is 50% less than the two samples of the same set. In the third set, the circular apertures of the same area that arranged in a square lattice are separate by $L = 0.8, 0.6,$ and $0.5\ mm$ for samples 7, 8, and 9 respectively that are corresponded to 375, 500, and 600 GHz respectively for the CNT-air interface. The area of this set is less than sample 1 by 50%. A unit cell of each sample is illustrated in Figure 4.1, and the parameters can be seen from Table 4.1. The first set of these samples was fabricated as transmission properties could be drawn from changing the area and the lattice arrangement for CNT-based EOT device with circular apertures. The CNTs of the samples are aligned single walled carbon nanotubes (SWCNT) on a high resistivity silicon substrate of $500\,\mu\mathrm{m}$ thickness that is transparent at THz. The density of the CNT film is 1×10^6 in a cross section of $1\,\mu\mathrm{m}^2$. The CNT was synthesized by arc-discharge, and the alignments is performed using slow vacuum filtration technique (30). At THz frequencies, the samples are mostly opaque when the alignment of the CNTs are parallel to the polarization of the incident wave, and it is significantly transparent when the alignment is perpendicular to the polarization of the incident wave. The experimental setup for the THz transmission measurment is shown in Figure 4.2. Each sample was rotated by 45° for each measurement in order to examine the lowest THz transmission with different alignments of the CNT's where the thin film scatter most of the incident beam.

4.2 Analysis of CNT-based EOT device

The time-domain terahertz transmission spectroscopy measurements of the highest transmission associated with the perpendicular orientation of the CNT's and the polarization of the THz beam is shown in Figure 4.3 as well as the lowest transmission associated with the parallel orientation of the CNT's and the polarization of the THz beam. The highest

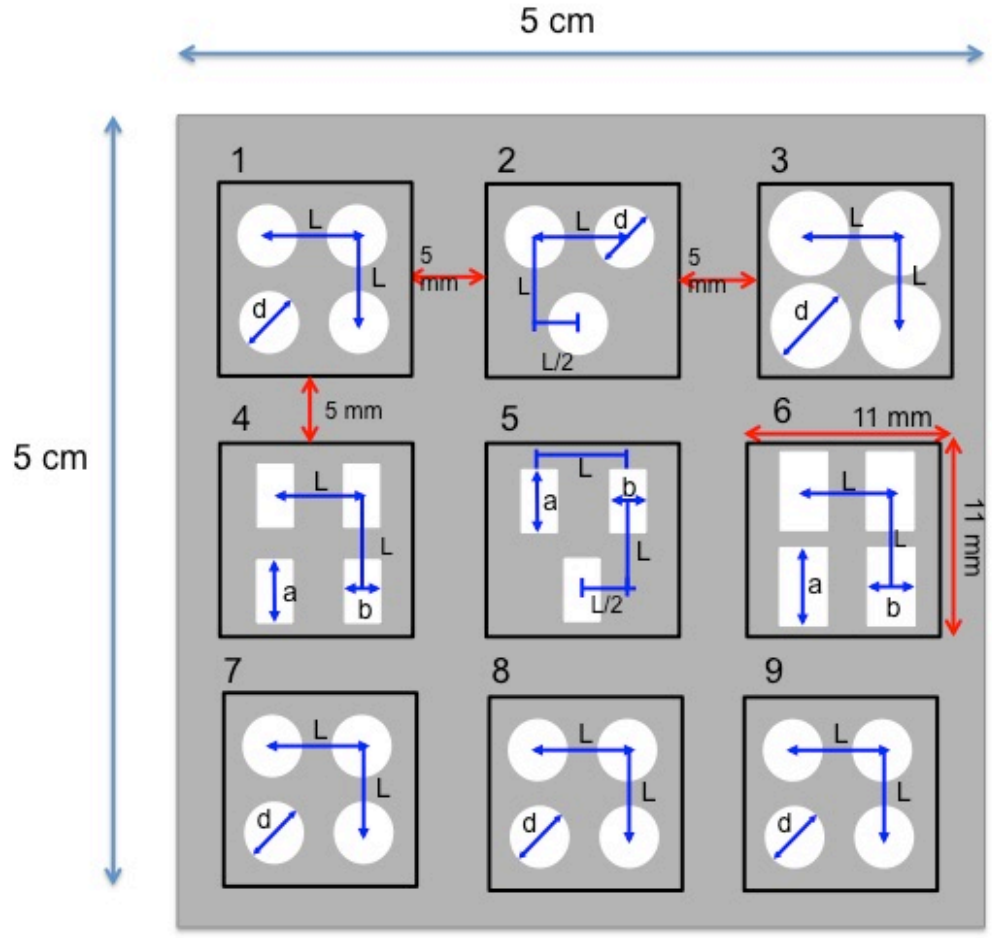

Figure 4.1: The first set (samples 1-3) has a circular aperture that arranged in square a lattice arrangement except for sample 2 that has a triangular lattice. The area of the first two samples of the first set are kept the same while the area of the third sample is about 50% bigger than the other samples of the same set. In the second set (samples4-6), all samples have rectangular apertures arranged in a square lattice except the second one of the same set that arranged in a triangular lattice. In this set, the area of the third sample is 50% less than the two samples of the same set. Samples 7-9, the circular apertures of the same area that arranged in a square lattice are separate by $L = 0.8, 0.6,$ and $0.5\ mm$ for samples 7, 8, and 9 respectively that are corresponding to 375, 500, and 600 GHz resonant frequency respectively. The area of this set is less than sample 1 by 50%. Each sample is centered in 11 mm by 11 mm square which fits the THz laser beam that has 10 mm diameter.

Sample	Aperture's shape	Aperture's dimensions (mm)	Area (mm^2)	Lattice arrangement	L (mm)
1	Circle	d= 0.54	0.229	square	1
2	Circle	d= 0.54	0.229	triangular	1
3	Circle	d= 0.65	0.332	square	1
4	Rectangular	a=0.533 b=0.133	0.071	square	1
5	Rectangular	a=0.533 b=0.133	0.071	triangular	1
6	Rectangular	a=0.1 b=0.4	0.04	square	1
7	Circle	d= 0.4	0.126	square	0.8
8	Circle	d= 0.4	0.126	square	0.6
9	Circle	d= 0.4	0.126	square	0.5

Table 4.1: Apertures shape and dimensions, lattice arrangement, area, and periodicity length for each sample.

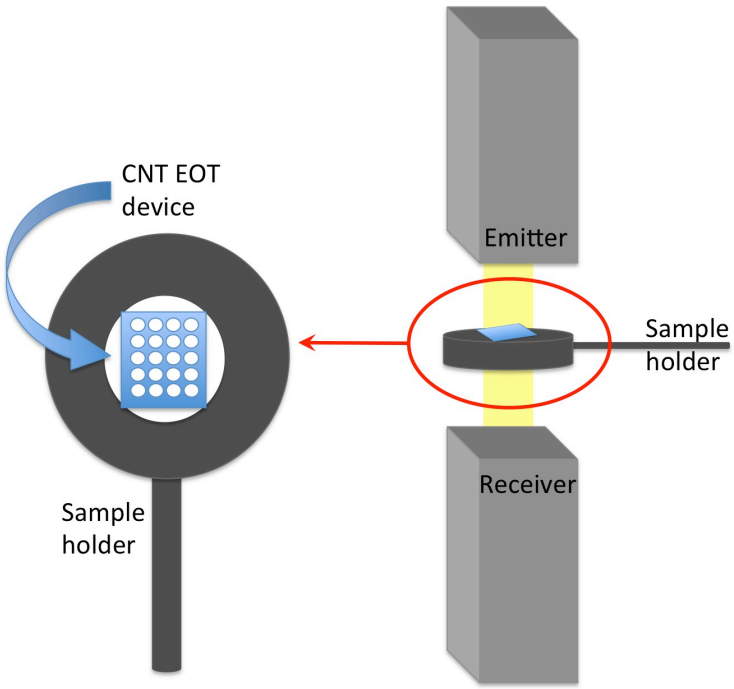

Figure 4.2: A scheme illustrates the THz transmission time domain spectroscopy. The THz beam size fits the EOT device.

transmission is slightly less than the transmission from the silicon which verifies the transparency of the thin film at this orientation. The orientation of the samples at the lowest and highest transmission is seen to be perpendicular which verifies the required alignment of the CNT thin film with the polarization of the THz beam. The time-domain terahertz transmission spectroscopy measurements for the reference (silicon) and the three samples with orientation that has the minimum transmission can be seen from Figure 4.4. The THz beam is attenuated differently across the three samples where it is more attenuated through the second sample. The transmission signal of the silicon substrate (reference), sample 1, sample, 2, and sample 3 is the first THz pulse. It can be seen from Figure 4.4 that the three EOT samples affect the presence of the secondary THz transmission that is always normally seen from a silicon wafer to etalon effects. The secondary transmission is almost completely minimized for all the three samples in the opaque orientation while it is seen for the silicon wafer and transparent orientation as in Figure 4.3. In order to verify the resonant frequency, the frequency domain representation of the spectroscopy data of the reference and samples are shown in Figure 4.5. The data analysis does not indicate any peak resonance at 300 GHz for the CNT-air interface or at 88 GHz associated with CNT-silicon interface, however; any such resonance might be weak due to thin nature of the samples. Similarly, plots of the transmission normalized to the reference so far show no resonant behavior as it can be seen from 4.6.

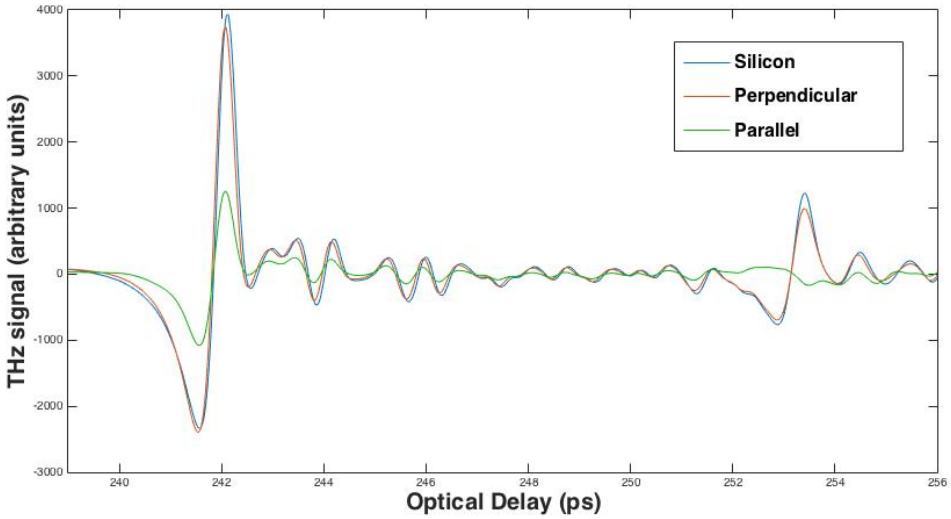

Figure 4.3: The time-domain terahertz transmission spectroscopy measurements of the silicon substrate (reference) and sample 2 with two orientations that show the maximum and minimum transmission associated with the orientation of the CNT's

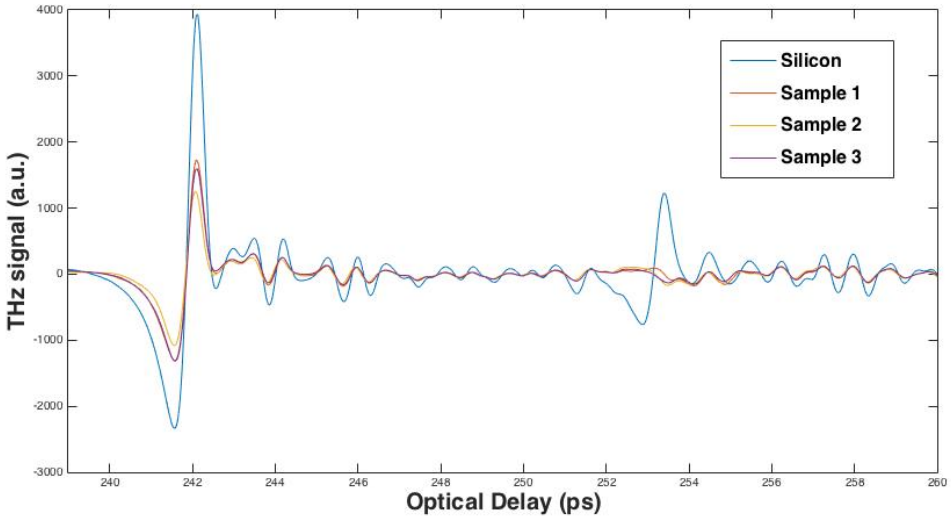

Figure 4.4: The time-domain terahertz transmission spectroscopy measurements of the silicon substrate (reference), sample 1, sample, 2, and sample 3.

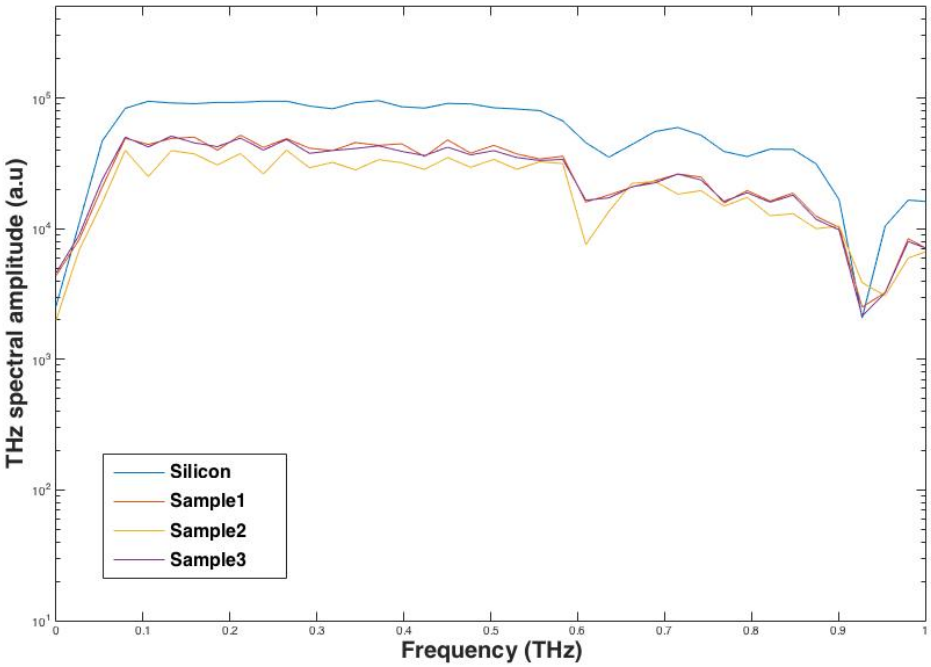

Figure 4.5: The THz frequency domain transmission spectroscopy measurements of the silicon substrate (reference), sample 1, sample, 2, and sample 3.

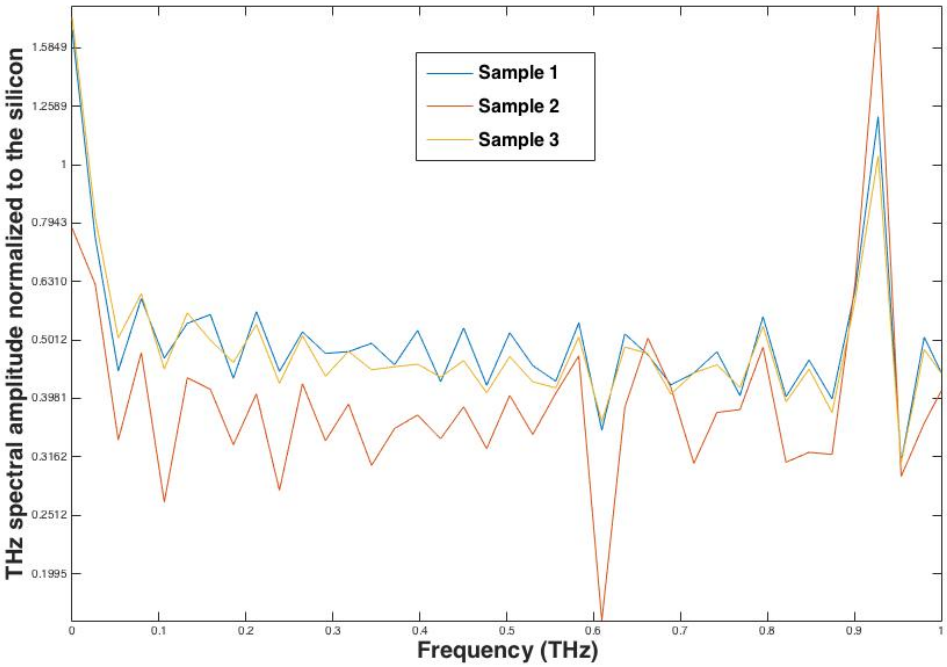

Figure 4.6: The THz frequency domain transmission spectroscopy measurements normalized to reference of sample 1, sample, 2, and sample 3.

Chapter 5

Summary and Outlook

In this work, the CNT-EOT device is studied computationally as a function of thickness and experimentally. Based on the simulated model, the transmission is consistent with the experiment reported in literature; however, Woods anomalies are seen in the modeled device only. Varying the thickness of the CNT-based EOT device shows good agreement with the experimental work in literature at THz frequencies where the transmission decays exponentially with increasing thickness. The calculated decay coefficient has its minimum value near resonance confirming the EOT phenomenon. At resonance, the transmission peak has its maximum value at the skin depth of the device ($40\,\mu\mathrm{m}$) followed by a decrease. The calculated critical length from the fitted data is $448\,\mu\mathrm{m}$ which is the largest thickness where the resonantly enhanced transmission is no longer supported.

Modeling of the critical thickness can be verified in future studies as well as the minimum thickness of CNT-EOT device providing a range of thicknesses that can be exploited in applications. Further, the impact of changing other factors such as the aperture shape, arrangement, and area providing a complete theoretical description of the behavior CNT-EOT device.

The aligned SWCNT thin film with 100 nm thickness EOT device does not indicate any

resonance; however any such resonance might be weak due to thin nature of the samples. Further polarization analysis could be taken in future as well as spectroscopic analysis of the optical properties of an aligned SWCNT thin film with 100 nm thickness which could lead to a better understanding of the behavior of such fabrication at THz frequencies of EOT devices. This experimental analysis could be used in modeling the EOT device in order to provide an optimum thickness for the aligned SWCNT thin film EOT devices.

Bibliography

[1] D. Graham-Rowe. Terahertz takes to the stage. *Nat Photon*, 1(2):75–77, 02 2007.

[2] M. Tonouchi. Cutting-edge terahertz technology. *Nat Photon*, 1(2):97–105, 02 2007.

[3] H. F. Ghaemi, T. Thio, D. E. Grupp, T. W. Ebbesen, and H. J. Lezec. Surface plasmons enhance optical transmission through subwavelength holes. *Phys. Rev. B*, 58:6779–6782, Sep 1998. doi: 10.1103/PhysRevB.58.6779. URL http://link.aps.org/doi/10.1103/PhysRevB.58.6779.

[4] A. J. Baragwanath, Mark Christopher Rosamond, Andrew James Gallant, and John Martyn Chamberlain. Time-of-flight model for the extraordinary transmission through periodic arrays of subwavelength apertures at thz frequencies. *Plasmonics*, 6(4):625, 2011. ISSN 1557-1963. doi: 10.1007/s11468-011-9244-1. URL http://dx.doi.org/10.1007/s11468-011-9244-1.

[5] S. A. Maier. *Plasmonics: Fundamentals and Applications*. Number 978-0-387-33150-8. Springer US, 2007.

[6] http://www.nature.com/nature/journal/v480/n7376/fig_tab/nature10610_F7.html. Accessed: 4/6/2017.

[7] J. Saxler. *Surface Plasmon Polaritons at Terahertz Frequencies on Metal and Semiconductor Surfaces*. PhD thesis, Aachen University, 2003.

[8] T. W. Ebbesen, H. J. Lezec, H. F. Ghaemi, T. Thio, and P. A. Wolff. Extraordinary optical transmission through sub-wavelength hole arrays. *Nature*, 391(6668):667–669, 02 1998. URL http://dx.doi.org/10.1038/35570.

[9] Y. Wang, Y. Tong, and X. Zhang. Transmission properties of terahertz waves through asymmetric rectangular aperture arrays on carbon nanotube films. *AIP Advances*, 6(4):045304, 2016. doi: 10.1063/1.4946787. URL http://dx.doi.org/10.1063/1.4946787.

[10] T. D. Nguyen, S. Liu, M. D. Lima, S. Fang, R. H. Baughman, A. Nahata, and Z. V. Vardeny. Terahertz surface plasmon polaritons on freestanding multi-walled carbon nanotube aerogel sheets. *Opt. Mater. Express*, 2(6):782–788, Jun 2012. doi: 10.1364/OME.2.000782. URL http://www.osapublishing.org/ome/abstract.cfm?URI=ome-2-6-782.

[11] Y. Wang, X. Zhao, G. Duan, and X. Zhang. Broadband extraordinary terahertz transmission through super-aligned carbon nanotubes film. *Opt. Express*, 24(14):15730–15741, Jul 2016. doi: 10.1364/OE.24.015730. URL http://www.opticsexpress.org/abstract.cfm?URI=oe-24-14-15730.

[12] S. Ganti. *Characterization and Modelling of Laser Micro-Machined Metallic Terahertz Wire Waveguides*. PhD thesis, Wright State University, 2012.

[13] D. H. Auston, K. P. Cheung, and P. R. Smith. Picosecond photoconducting Hertzian dipoles. *Applied Physics Letters*, 45:284–286, August 1984. doi: 10.1063/1.95174.

[14] L. Yun-Shik. *Principles of Terahertz Science and Technology*. Springer US, 2009.

[15] M. A. Ordal, Robert J. Bell, R. W. Alexander, L. L. Long, and M. R. Querry. Optical properties of fourteen metals in the infrared and far infrared: Al, co, cu, au, fe, pb, mo, ni, pd, pt, ag, ti, v, and w. *Appl. Opt.*, 24(24):4493–4499, Dec 1985. doi: 10.1364/AO.24.004493. URL http://ao.osa.org/abstract.cfm?URI=ao-24-24-4493.

[16] F. L. Pedrotti, L. M. Pedrotti, and L. S. Pedrotti. *Introduction to Optics*. Pearson Prentice Hall, third edition edition, 2006.

[17] A. Azad and W. Zhang. Resonant terahertz transmission in subwavelength metallic hole arrays of sub-skin-depth thickness. *Opt. Lett.*, 30(21):2945–2947, Nov 2005. doi: 10.1364/OL.30.002945. URL http://ol.osa.org/abstract.cfm?URI=ol-30-21-2945.

[18] T. J. Kim, T. Thio, T. W. Ebbesen, D. E. Grupp, and H. J. Lezec. Control of optical transmission through metals perforated with subwavelength hole arrays. *Opt. Lett.*, 24 (4):256–258, Feb 1999. doi: 10.1364/OL.24.000256. URL http://ol.osa.org/abstract.cfm?URI=ol-24-4-256.

[19] James V. Coe, Joseph M. Heer, Shannon Teeters-Kennedy, Hong Tian, and Kenneth R. Rodriguez. Extraordinary transmission of metal films with arrays of subwavelength holes. *Annual Review of Physical Chemistry*, 59(1):179–202, 2008. doi: 10.1146/annurev.physchem.59.032607.093703. URL http://dx.doi.org/10.1146/annurev.physchem.59.032607.093703. PMID: 17988200.

[20] L. Martín-Moreno, F. J. García-Vidal, H. J. Lezec, K. M. Pellerin, T. Thio, J. B. Pendry, and T. W. Ebbesen. Theory of extraordinary optical transmission through subwavelength hole arrays. *Phys. Rev. Lett.*, 86:1114–1117, Feb 2001. doi: 10.1103/PhysRevLett.86.1114. URL http://link.aps.org/doi/10.1103/PhysRevLett.86.1114.

[21] A. Degiron, H. J. Lezec, W. L. Barnes, and T. W. Ebbesen. Effects of hole depth on enhanced light transmission through subwavelength hole arrays. *Applied Physics Letters*, 81(23):4327–4329, 2002. doi: 10.1063/1.1526162. URL http://dx.doi.org/10.1063/1.1526162.

[22] C. Janke, J. Gómez Rivas, C. Schotsch, L. Beckmann, P. Haring Bolivar, and H. Kurz. Optimization of enhanced terahertz transmission through arrays of subwavelength

apertures. *Phys. Rev. B*, 69:205314, May 2004. doi: 10.1103/PhysRevB.69.205314. URL http://link.aps.org/doi/10.1103/PhysRevB.69.205314.

[23] X. Shou, A. Agrawal, and A. Nahata. Role of metal film thickness on the enhanced transmission properties of a periodic array of subwavelength apertures. *Opt. Express*, 13(24):9834–9840, Nov 2005. doi: 10.1364/OPEX.13.009834. URL http://www.opticsexpress.org/abstract.cfm?URI=oe-13-24-9834.

[24] S. M. Musa, A.V. Kulkarni, and V.K. Havanur. *Finite Element Analysis*. Mercury Learning and Information, 2014.

[25] J. A. Deibel, M. Escarra, N. Berndsen, K. Wang, and D. M. Mittleman. Finite-element method simulations of guided wave phenomena at terahertz frequencies. *Proceedings of the IEEE*, 95(8):1624–1640, Aug 2007. ISSN 0018-9219. doi: 10.1109/JPROC.2007.898817.

[26] https://www.comsol.com/rf-module. Accessed: 4/4/2017.

[27] A. Z. Elsherbeni and V. Demir. *The Finite-Difference Time-Domain method for Electromagnetics with Matlab Simulations*. SciTech Publishing, Inc, 2009.

[28] https://lost-contact.mit.edu/afs/pdc.kth.se/roots/ilse/v0.7/pdc/vol/comsol/3.2/amd64_fc3/doc/em/wwhelp/wwhimpl/common/html/wwhelp.htm?context=em&file=modeling-09.html. Accessed: 4/4/2017.

[29] https://www.comsol.com/blogs/modeling-metallic-objects-in-wave-electromagnetics\-problems/. Accessed: 4/4/2017.

[30] X. He, W. Gao, L. Xie, B. Li, Q. Zhang, S. Lei, J. M. Robinson, E. H. Hároz, S. K. Doorn, W. Wang, R. Vajtai, P. M. Ajayan, W. W. Adams, R. H. Hauge, and J. Kono. Wafer-scale monodomain films of spontaneously aligned single-walled carbon nan-

otubes. *Nat Nano*, 11(7):633–638, 07 2016. URL http://dx.doi.org/10.1038/nnano.2016.44.